

## Photometric Analysis of the OGLE Heartbeat Stars

MARCIN WRONA,<sup>1</sup> PIOTR A. KOŁACZEK-SZYMAŃSKI,<sup>2</sup> MILENA RATAJCZAK,<sup>1</sup> AND SZYMON KOZŁOWSKI<sup>1</sup>

<sup>1</sup>*Astronomical Observatory, University of Warsaw, Al. Ujazdowskie 4, 00-478 Warszawa, Poland*

<sup>2</sup>*Astronomical Institute, University of Wrocław, Kopernika 11, 51-622 Wrocław, Poland*

### ABSTRACT

We present an analysis of 991 heartbeat stars (HBSs) from the OGLE Collection of Variable Stars (OCVS). The sample consists of 512 objects located toward the Galactic bulge (GB), 439 in the Large Magellanic Cloud (LMC) and 40 in the Small Magellanic Cloud (SMC). We model the *I*-band OGLE light curves using an analytical model of flux variations, reflecting tidal deformations between stars. We present distributions of the model parameters that include the eccentricity, orbital inclination, and argument of the periastron, but also the period-amplitude diagrams. On the Hertzsprung-Russell (HR) diagram, our HBS sample forms two separate groups of different evolutionary status. The first group of about 90 systems, with short orbital periods ( $P \lesssim 50$  days), consists of an early-type primary star lying on (or close to) the main sequence (MS). The second group of about 900 systems, with long orbital periods ( $P \gtrsim 100$  days), contains a red giant (RG). The position of RG HBSs on the period-luminosity diagram strongly indicates their binary nature. They appear to be a natural extension of confirmed binary systems that include the OGLE ellipsoidal and Long Secondary Period (LSP) variables. We also present a time-series analysis leading to detection of tidally-excited oscillations (TEOs). We identify such pulsations in about 5% of stars in the sample with a total number of 78 different modes. This first relatively large homogeneous sample of TEOs allowed us to construct a diagram revealing the correlation between the TEO's orbital harmonic number and the eccentricity of the host binary system.

*Keywords:* binaries: general; stars: oscillations (including pulsations); stars: variables: general;

### 1. INTRODUCTION

Heartbeat stars (hereafter HBSs) are a subclass of ellipsoidal variable stars with eccentric orbits. The ellipsoidal variable stars are close binary systems whose components are deformed due to gravitational tidal forces. For a "classical" ellipsoidal variable, which typically has a circular orbit, the light curve is characterized by a sinusoidal-like shape with two maxima and two minima per orbital period. This is a result of observing different sides of the stellar surface, which is distorted into rotational ellipsoid (Morris 1985).

If the orbit of the system is eccentric, the deformation strength depends on the orbital phase and the strongest effect appears during the periastron passage. This variation of the tidal force affects the shape of the light curve,

which starts to deviate from the typical sinusoidal-like shape. The response of the stellar surface and volume to the presence of varying tidal potential can be expressed as a sum of two effects (Zahn 1975). The first one is an equilibrium tide which refers to the instantaneous deformation of a star due to tides. It is the only component of the tidal response provided that the system is a circular and synchronized binary. The equilibrium tide is responsible for the presence of the "heartbeat" feature in the light curves of HBSs. This prominent characteristic reminds a single electrocardiogram pulse, hence the name of this group of variables. For HBSs there is no strict limit on eccentricity where systems begin to be considered as an HBS, but as we show in our analysis, there are only a few HBSs with  $e \lesssim 0.1$ .

The second type of the stellar tidal response is the dynamical tide which may manifest itself as tidally-excited oscillations (hereafter TEOs; e.g., Zahn 1970, Kumar et al. 1995, Fuller 2017). The periodically changing tidal potential may act as the driving force and induce even

naturally damped pulsations, which would not be visible in the absence of a nearby companion. Most of the TEOs observed in main-sequence (MS) stars are high-radial order gravity modes (Guo 2021).

Kumar et al. (1995) provided a convenient analytical model (we will refer to it as the Kumar’s model) of the flux variations driven by tidal interactions. The Kumar’s model allows for determination of orbital parameters of the system, based only on the shape of the single-passband light curve. For instance, this model was successfully applied to derive orbital parameters for a sample of HBSs discovered by Thompson et al. (2012). The Kumar’s model accounts only for ellipsoidal variability. It neglects other proximity effects like irradiation/reflection effect and Doppler beaming/boosting. While the latter one should not be pronounced in our sample of HBSs because of their long orbital periods and hence low radial velocities, the former effect may play a potentially significant role.

The prototype of entire HBSs class is KOI-54 (HD 187091), studied in detail by many authors, e.g., Welsh et al. (2011), Burkart et al. (2012), Fuller & Lai (2012). For the first time, the HBS was reported as a separate class of variable stars in the work of Thompson et al. (2012), but such objects were known in the literature much earlier (e.g., Handler et al. 2002, Maceroni et al. 2009). A group of more than 100 ellipsoidal variables with an eccentric orbit was highlighted in the work of Soszyński et al. (2004). A subsample of them were analyzed later by Nicholls et al. (2010, 2012) and Nie et al. (2017). Their studies showed that HBSs containing a red giant (RG) have typically longer periods than classical ellipsoidal variables. In our sample of HBSs, the vast majority of them are representative of such systems, therefore we could verify that HBSs are indeed an extension of the classical ellipsoidal systems to longer periods for a given brightness.

Most of the papers on HBSs published so far focused on individual objects, e.g., KOI-54 (Welsh et al. 2011), KIC 3749404 (Hambleton et al. 2016), KIC 8164262 (Hambleton et al. 2018), MACHO80.7443.1717 (OGLE-LMC-HB-0254; Jayasinghe et al. 2019, 2021). Due to the limited number of known HBSs, the detailed quantitative analysis has been challenging to carry out. A sketchy analysis of HBSs containing RG stars was conducted firstly in the work of Soszyński et al. (2004), where authors explained the reason for the unusual shape of the light curves of the ellipsoidal variables. Later, a subset of those systems were analyzed by Nicholls & Wood (2012) and then by Nie & Wood (2014). In both works, authors measured changes in radial velocities confirming the binary nature of those

stars, and showing that the strongest brightness changes occur near the periastron passage. Afterward, Nie et al. (2017) presented an analysis of 81 ellipsoidal RG stars including 22 HBSs. They mainly focused on the evolutionary status of those stars and the primary/secondary mass distributions. In turn, Beck et al. (2014) studied asteroseismic properties of 18 RG HBSs found in the data obtained by NASA’s Kepler Space Telescope (Borucki et al. 2010).

Another set of HBSs, but consisting of stars located on or close to the MS, was found also in the Kepler database (17 objects were the subject of an analysis by Thompson et al. 2012). The catalog including HBSs among other variable stars was released by Kirk et al. (2016). Those HBSs are mainly low- and intermediate-mass A-F-type stars. They are characterized by a short orbital period (days to tens of days) and very small amplitudes of brightness variations (a few millimagnitudes) contrary to the HBSs with an RG star, which have much longer periods (hundreds of days) and an order of magnitude higher amplitudes.

Recently, using The 9th Catalogue of Spectroscopic Binary Orbits (Pourbaix et al. 2004), Kołaczek-Szymański et al. (2021) selected HBS candidates and examined their light curves delivered by the Transiting Exoplanet Survey Satellite mission from sectors 1–16 (mostly the southern ecliptic hemisphere). The authors discovered 20 massive and intermediate-mass HBSs, seven of which exhibit several TEOs lying at low harmonics of the orbital frequency.

In this work, we will conduct a general analysis of 991 HBSs cataloged in the OGLE Collection of Variable Stars (OCVS; Wrona et al. 2021). In parallel to the analysis of the heartbeat phenomenon itself, we will search for TEOs in the presented collection of the OGLE HBSs. The derived sample of binaries exhibiting TEOs may be a valuable testbed for future studies on the influence of dynamical tides on the orbital evolution in binary systems, including those with evolved companions.

The structure of this paper is as follows. In Section 2, we describe the origin of the photometric data of the HBSs and the way how we prepare them for the examination. In Section 3, we describe the modeling process of the light curves using the Kumar’s model. In Section 4, we introduce the methodology of search for TEOs. The core of our work is presented in Section 5, where we discuss the results of the analysis. In Section 6, we conclude our work.

## 2. PHOTOMETRIC DATA

In this work, we analyze the sample of HBSs found in the OGLE project database. The detailed specification of the data is presented in Section 2 of the catalog paper (Wrona et al. 2021).

Time-series data used in the analysis were obtained using the 1.3-m Warsaw Telescope located at Las Campanas Observatory, Chile. The majority of the data come from the fourth phase of the OGLE project, in operation since 2010 (Udalski et al. 2015). The observations were conducted using Cousins  $I$ -band and Johnson  $V$ -band filters. The photometry was obtained using Differential Image Analysis (e.g., Alard & Lupton 1998, Woźniak 2000). All the data for each filter were calibrated separately to the standard photometric system using the scheme presented by Udalski et al. (2015). We also corrected the photometric uncertainties based on work of Skowron et al. (2016).

In the analysis and modeling of the light curves, we used mainly the  $I$ -band data. The  $V$ -band photometry was used to determine the  $(V - I)$  color information for all HBSs from our sample. To prepare the data for modeling and analysis we have taken the following steps.

First, we cleared the light curves from outliers by rejecting all the data which lied outside  $3\sigma$  level from the average flux, where  $\sigma$  is the standard deviation of flux. This step was taken separately for all the available data obtained by different OGLE phases (OGLE-II, OGLE-III, OGLE-IV) because in some cases there was a significant shift in the mean flux between those data. During this step, we also removed sets of data consisting of clearly improperly determined photometry, which could be caused for instance by bad weather conditions during the observing night or some failure in the DIA pipeline (this is a very common case for sources with high proper motions).

The second step was to remove trends in the data sets. This procedure was done separately for data obtained during OGLE-II, OGLE-III and OGLE-IV. To each part of the light curve, we fitted splines. Then, obtained sets of splines were subtracted from the data.

In the third step, we shifted the detrended data from the OGLE-II and OGLE-III to the OGLE-IV (or to the OGLE-III if there was no data from the OGLE-IV). For this purpose, we calculated the mean flux for each phase and we shifted the data to the latest phase by the difference between these averages.

Finally, we used additional cleaning procedures. Using the combined data from all phases, we prepared light curves phase-folded with the orbital period and we divided them into bins, which width was set on 0.1 of the orbital phase. Then we calculated a standard deviation in each bin and we removed points that lied more than

$A \cdot \sigma$  from the mean magnitude. The  $A$  parameter was chosen individually for each star and it mainly depended on the number and positions of outlying points. The  $A$  parameter usually was about 3.

To assess photometric temperatures for the HBSs containing a hot primary we used  $UBV$  photometry obtained by Massey (2002). Data were taken with the Curtis Schmidt telescope at Cerro Tololo Inter-American Observatory (CTIO), Chile, using a Tektronix  $2048 \times 2048$  CCD with  $2.32''/\text{pixel}$  scale. Observations were made at the beginning of 1999 and in 2001 March/April.

For some objects the aforementioned  $UBV$  data were unavailable and therefore we decided to use  $UBV$  photometry obtained by Zaritsky et al. (2004). The authors used the 1-m Swope Telescope, located at Las Campanas Observatory, right next to the Warsaw Telescope. Observations were taken with the Great Circle Camera with a 2K CCD, with a  $0.7''$  pixel scale, between 1995 October and 1999 December, and with additional observations in 2001 December.

In this work, we also present, among others, period-luminosity diagrams using the  $W_{JK}$  Wesenheit index. To calculate this quantity, we used  $JHK_s$  photometry collected by Kato et al. (2007), using the InfraRed Survey Facility (IRSF) 1.4-m telescope at Sutherland, the South African Astronomical Observatory, with SIR-IUS camera, which is equipped with three  $1024 \times 1024$  HAWAII. The pixel scale for this camera is  $0.45''$ .

As complementary data, we utilized photometry collected during the Two Micron All Sky Survey (2MASS) (Skrutskie et al. 2006). 2MASS used two 1.3-m telescopes located at Mount Hopkins, Arizona, and at the CTIO, Chile. The telescopes were equipped with three NICMOS3  $256 \times 256$  HgCdTe arrays with pixel size equals to  $2''$ . Observations were taken between 1997 June and 2001 February.

### 3. MODELING

#### 3.1. The Kumar's model of a light curve

In this work, we decided to use the analytic model of tidally induced stellar deformation, presented in Kumar et al. (1995), where the flux variations are described by their Equation (44). The Kumar's model was derived under certain assumptions and simplifications, such as: assuming the spin-orbit alignment, including only dominant modes (spherical harmonics with  $l = 2$ ,  $m = 0, \pm 2$ ), aligning the tidal bulge with the line connecting mass centers of stars, neglecting irradiation and Doppler beaming effects. Therefore, even a perfectly fitted model to the light curve gives only an assessment of the orbital parameters. The slightly modified version of the Kumar's formula was successfully used by many au-

thors (e.g., Thompson et al. 2012, Jayasinghe et al. 2019, Kołaczek-Szymański et al. 2021) to assess basic orbital parameters of the system, based on the light curve. According to Thompson et al. (2012), the relative change of the flux caused by tidal deformation as a function of time  $t$  can be expressed as:

$$\frac{\delta F}{F}(t) = S \cdot \frac{1 - 3 \sin^3 i \sin^2(\varphi(t) - \omega)}{(R(t)/a)^3} + C, \quad (1)$$

where  $S$  is the scaling factor of the amplitude,  $C$  is the zero-point offset,  $i$  is the inclination of the orbit,  $\omega$  is the argument of the periastron,  $\varphi(t)$  represents the true anomaly as a function of time,  $R(t)$  describes the distance between components of the system as a function of time, and  $a$  is the semimajor axis.

Both time-dependent variables  $(R(t)/a)$  and  $\varphi(t)$  can be re-written as functions of the eccentricity  $e$  and eccentric anomaly  $E$ :

$$\frac{R(t)}{a} = 1 - e \cos E(t), \quad (2)$$

$$\varphi(t) = 2 \arctan \left( \sqrt{\frac{1+e}{1-e}} \cdot \tan \left( \frac{E(t)}{2} \right) \right). \quad (3)$$

The eccentric anomaly  $E$  and the time  $t$  are connected by Kepler's equation:

$$\frac{2\pi(t - T_0)}{P} = E - e \sin E, \quad (4)$$

where  $T_0$  is the time of periastron passage and  $P$  is the orbital period.

However, we believe that there is a faultiness in Equation (1). In the top panel of Figure 1, we present the light curve of the HBS named OGLE-BLG-HB-0081. In the modeling process, we used Equation (1) and Markov Chain Monte Carlo (MCMC) fitting procedure (described in more detail in Section 3.2). We obtained the following orbital parameters:  $e_K = 0.803$ ,  $i_K = 64^\circ$  and  $\omega_K = 17^\circ$ . The fitted model is represented by the red line in Figure 1. We also performed modeling of that light curve using the PHysics Of Eclipsing BinariEs (PHEOBE) Legacy program<sup>1</sup> (Prša & Zwitter 2005), which is based on the Wilson-Devinney (WD) code (Wilson & Devinney 1971), thus it is independent of the Kumar's model. The resulting values of  $e_{WD} = 0.78$  and  $i_{WD} = 55^\circ$  are similar to the ones obtained with the Kumar's model (within  $3\sigma$ ), but the argument of periastron is far from that:  $\omega_{WD} = 152^\circ$ . Setting these values to Equation (1) and plotting results in Figure 1 we got the

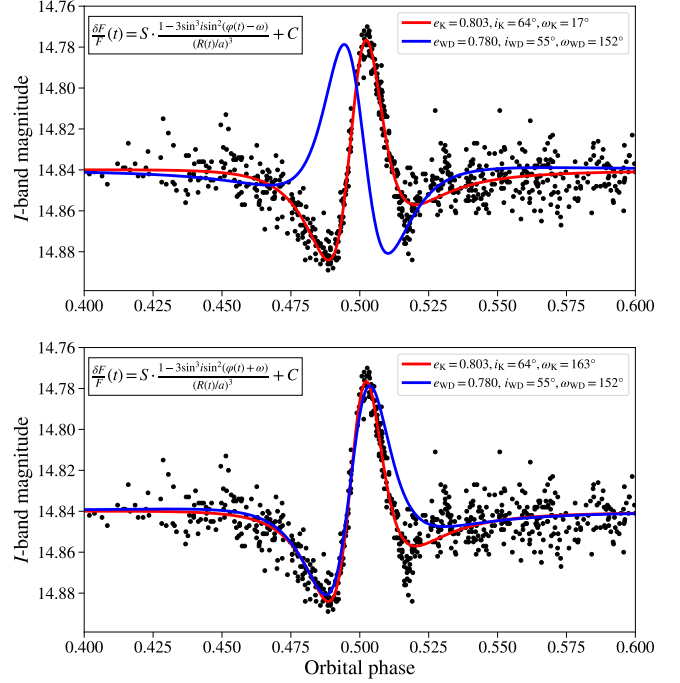


**Figure 1.** Phase-folded light curve of the OGLE-BLG-HB-0081 (black dots). In the top panel, we plot lines based on the Kumar's model described by Equation (1), while in the bottom panel we used the corrected version shown in Equation (5). We obtained orbital parameters of the system using two independent methods – the Kumar's model (red line, index K) and the PHEOBE Legacy program which is based on the WD code (blue line, index WD). Both methods produce similar results only if we use the corrected version of the Kumar's model, presented in Equation (5).

blue line. It is clearly seen that this model is far from being proper, but one can notice that the blue line is a symmetric reflection of the red one about the vertical axis.

We also compared light curves generated on the basis of Equation (1) with synthetic light curves presented in Figure 5 in the work of Thompson et al. (2012). The results turned out to be very similar to the ones described above. Our light curves were symmetric reflections of the ones presented by Thompson et al. (2012). We are certain that the fault is connected with the sign of the  $\omega$  in Equation (1) because by inverting this sign we get proper models. The source of this discrepancy is elusive. Nevertheless, the version of Equation (1) with plus sign before  $\omega$  makes the model fit properly to the data and it is in agreement with synthetic light curves generated with alternative methods, thus we decided to use the following equation instead of Equation (1):

$$\frac{\delta F}{F}(t) = S \cdot \frac{1 - 3 \sin^3 i \sin^2(\varphi(t) + \omega)}{(R(t)/a)^3} + C, \quad (5)$$

<sup>1</sup> <http://phoebe-project.org/>



The default unit of a star’s brightness in our catalog is magnitude, while during the modeling we operated with fractional change of the flux. We can express the change of the magnitude using the Pogson’s equation:

$$\begin{aligned}\delta m = m - m_0 &= -2.5 \log_{10} \left( \frac{F + \delta F}{F} \right) = \\ &= -2.5 \log_{10} \left( 1 + \frac{\delta F}{F} \right),\end{aligned}\quad (6)$$

where we used the median magnitude as a zero-point,  $m_0$ . Thus, we can calculate the fractional change of the flux using following formula:

$$\frac{\delta F}{F} = 10^{-0.4(m - m_0)} - 1, \quad (7)$$

$$\sigma_f = \frac{2.5(\delta F/F)\sigma_m}{\ln 10}, \quad (8)$$

where  $\sigma_f$  is an uncertainty of the flux change with a given uncertainty of the magnitude change,  $\sigma_m$ .

### 3.2. Fitting the Kumar’s model to the light curve

In the fitting procedure, we decided to use the MCMC method, firstly to search for a proper model and to investigate plausible degeneracies, and secondly to estimate uncertainties of the model’s parameters. We used Python’s `emcee` v3.0.2 package, described in detail in Foreman-Mackey et al. (2013).

The time span of the OGLE HBS light curves often exceeds a dozen years, therefore in the case of a high apsidal motion rate, the shape of the light curve can change significantly. That may degrade the quality of the Kumar’s model fit. To estimate the role of apsidal motion, we compared phase-folded light curves from the first and last three observational seasons. We did not detect any significant changes in the shape of light curves for the vast majority of HBSs, thus we decided to skip the apsidal motion in the fitting procedure.

#### 3.2.1. Uniqueness of the solution found using the Kumar’s model

To assess the risk of degeneracy of the Kumar’s model, we created 100 synthetic light curves with randomly selected parameters from the entire hyperspace. We also took into account the noise of the brightness and the uneven time sampling for the typical OGLE light curve. We assumed the normal distribution of the noise with the standard deviation depending on the mean magnitude, which was also randomly selected. The time sampling included the mid-season gaps and typical cadence of the observations for the central regions of the Magellanic Clouds (MCs) during the OGLE-IV project.

In the fitting process we used MCMC method. In the MCMC run, we used the Kumar’s model, according

to the formulas introduced in Section 3.1. We adopted the flat prior distribution for  $e$ ,  $i$  and  $\omega$ . We limited their final values to the physically reasonable range, but with a small margin for angular variables to avoid sharp cuts at the final distribution:  $0 < e < 1$ ,  $0^\circ < i < 92^\circ$ ,  $-10^\circ < \omega < 190^\circ$ . The range of the argument of periastron is only a half of the full angle because the stellar distortion due to tidal deformation is symmetric along the elongation axis. For the remaining parameters we used the normal prior distribution. The range limit for  $P$  and  $T_0$  were connected to their estimated initial values  $P_e$ ,  $T_{0,e}$ :  $0.95P_e < P < 1.05P_e$ ,  $T_{0,e} - 0.5P_e < T_0 < T_{0,e} + 0.5P_e$ . In the modeling process, we used 50 walkers and 20 000 steps for a single chain. The final value of each parameter was the median of the resulted distribution.

Only in 4 out of 100 simulated light curves, we did not recover the initial Kumar’s model parameters. In one case, the program found two equivalent solutions for  $\omega$ , one about  $0^\circ$  and the second about  $180^\circ$ . Those two solutions are indistinguishable mathematically because of the periodicity of the  $\sin^2(\varphi(t) + \omega)$  part of the Kumar’s model. In another case, the program bounced between two values of the orbital period – the proper value and the unexpected one, with the dominance of the second one. In the remaining two cases, both final solutions were degenerate, but always one of the degeneracies was the correct solution. For 96 simulated light curves, the MCMC fitting procedure returned proper values of parameters within the one sigma region.

#### 3.2.2. Modeling of the OGLE HBSs light curves

We conducted fitting with the MCMC method for all 991 HBSs from our sample. We used cleaned, detrended, and adjusted to the latest OGLE phase light curves, as described in Section 2. Stars with additional brightness variations such as eclipses or spots, were manually cleaned by removing the affected part of the light curve if it could be easily separated from the heartbeat modulation. Nevertheless, in some cases this procedure could affect the heartbeat shape, therefore the final parameters may not be reliable. Each OGLE HBS for which we did not find proper Kumar’s model or the fitted model is unreliable, has been appropriately flagged (cf., description of Table A2 of the catalog paper by Wrona et al. 2021).

We run the fitting process with similar prior distributions of parameters and their limits as described in Section 3.2.1. We calculated initial orbital periods,  $P_e$  using the FNPEAKS<sup>2</sup> program, which is based on Fourier fre-

<sup>2</sup> <http://helas.astro.uni.wroc.pl/deliverables.php?active=fnpeaks>

quency spectra. The initial time of periastron passage,  $T_{0,e}$  was estimated based on the local extrema in the light curves.

In the MCMC fitting process, for each star, we applied 50 walkers with 20 000 steps in a single chain. Only about 6% of the HBSs showed signs of degeneracies. In most cases, the problems were  $\omega$  bouncing between  $0^\circ$  and  $180^\circ$  or the program finding a different solution for the period. For those problematic stars, we used another MCMC run, with a larger number of walkers and steps and with narrower prior distributions. This approach leads to proper models for most of the troublesome light curves. We could not find the satisfactory model only for about 2% of our HBSs.

Finally, we once more used MCMC fitting to properly estimate the uncertainties of Kumar’s parameters. The priors were randomly selected using a normal distribution centered on the value from the previous step and the standard deviation being one-hundredth of this value (for  $T_0$  we used  $P/100$  and for  $C$  we used  $C/1000$ ). We used 100 walkers and 25 000 steps in a single chain.

As a final value of the given parameter, we used the maximum value of the distribution, instead of the median value. In most cases, these two give similar values, but for the non-Gaussian distribution (e.g., when  $i$  value is about  $90^\circ$ ), we found that the first one results in better-fitted models. As uncertainties  $\sigma_-$  and  $\sigma_+$  we assigned distances between the 50th and the 16th and 84th percentile of the distribution, respectively. In Figure 2, we present a typical corner plot (top panel) and the corresponding phase-folded light curve including the model (bottom panel). Both corner plots and light curves with the fitted model for each OGLE HBS are available on the OGLE websites<sup>3</sup>. In most cases there are no clearly visible correlations between parameters, except for the following pairs:  $i - S$ ,  $i - C$ ,  $\omega - T_0$ , and less often  $P - T_0$ .

The final values of the Kumar’s model parameters for each star with their uncertainties are presented in the catalog paper (Wrona et al. 2021, their Table A3).

## 4. TIDALLY-EXCITED OSCILLATIONS

### 4.1. General properties of TEOs

The majority of TEOs are forced damped gravity modes which may dissipate the total orbital energy and make the system tighter with time. Therefore, TEOs may play a significant role in the dynamical evolution of the binary system. In general, TEOs come in two

”varieties”. The first one occurs when the frequency of the normal eigenmode of pulsation temporarily coincides with the harmonic,  $n$  of the orbital frequency,  $f_{\text{orb}}$ . In such circumstances, which are called a ”chance resonance”, the amplitude of a TEO does not exceed parts per thousand (ppt) level and most often is orders of magnitude smaller. The other variety is associated with the so-called ”resonantly-locked modes” (cf., Fuller 2017, Hambleton et al. 2018). These are forced normal modes with frequencies evolving due to stellar evolution at the same rate and direction as harmonic of the orbital frequency. Therefore, resonantly-locked TEOs have enough time to gain relatively high amplitudes, hence effectively dissipate the total orbital energy. High-amplitude TEOs are expected to be quadrupole ( $l = 2$ ) modes with azimuthal order  $m = 0$ , or 2. Although the history of theoretical studies of dynamical tides dates back to the 70’s (Zahn 1970), the actual effectiveness of energy dissipation due to TEOs and their impact on binary’s evolution is still a matter of large uncertainties. Studies of large-amplitude TEOs offer a unique opportunity to make progress in this subject.

The main observational difference between self-excited pulsations and TEOs is that the latter ones have frequencies exactly equal to integer multiples of  $f_{\text{orb}}$ , therefore they phase well with the orbital period,  $P$ . Nevertheless, because of the non-linear mode coupling (hereafter NLMC, described extensively, for instance by Dziembowski 1982) it is possible to observe also non-harmonic TEOs which are ”daughter” modes of the resonant (harmonic) TEO being a ”mother” mode (e.g., Guo 2020). The simplest manifestation of this mechanism is the decay of resonant TEO into two modes, the sum of the frequencies of which equal to  $n \cdot f_{\text{orb}}$ . However, in general, one can also expect the quintuplets, septuplets, etc. of frequencies formed via higher-order NLMC and/or non-harmonic TEOs being e.g. a ”grand-daughter”, ”great-granddaughter”, etc. modes.

There are several other features that make TEOs unique when compared to self-excited modes. Therefore, one can talk about the whole branch of the so-called ”tidal asteroseismology”. One of the most extensively studied HBS in terms of tidal asteroseismology is the aforementioned KOI-54, for which this type of analysis was performed by Burkart et al. (2012). There are also other papers dedicated solely to this topic like e.g. Guo et al. (2020).

### 4.2. Methodology of search

We search for TEOs in our sample of HBSs by means of the Fourier analysis. We performed a standard iterative pre-whitening procedure on the residual light curves

<sup>3</sup> <http://www.astrouw.edu.pl/ogle/ogle4/OCVS/blg/hb/> - for the GB sample of HBSs (instead ”blg” use ”lmc” or ”smc” for the LMC or SMC sample of HBSs, respectively).

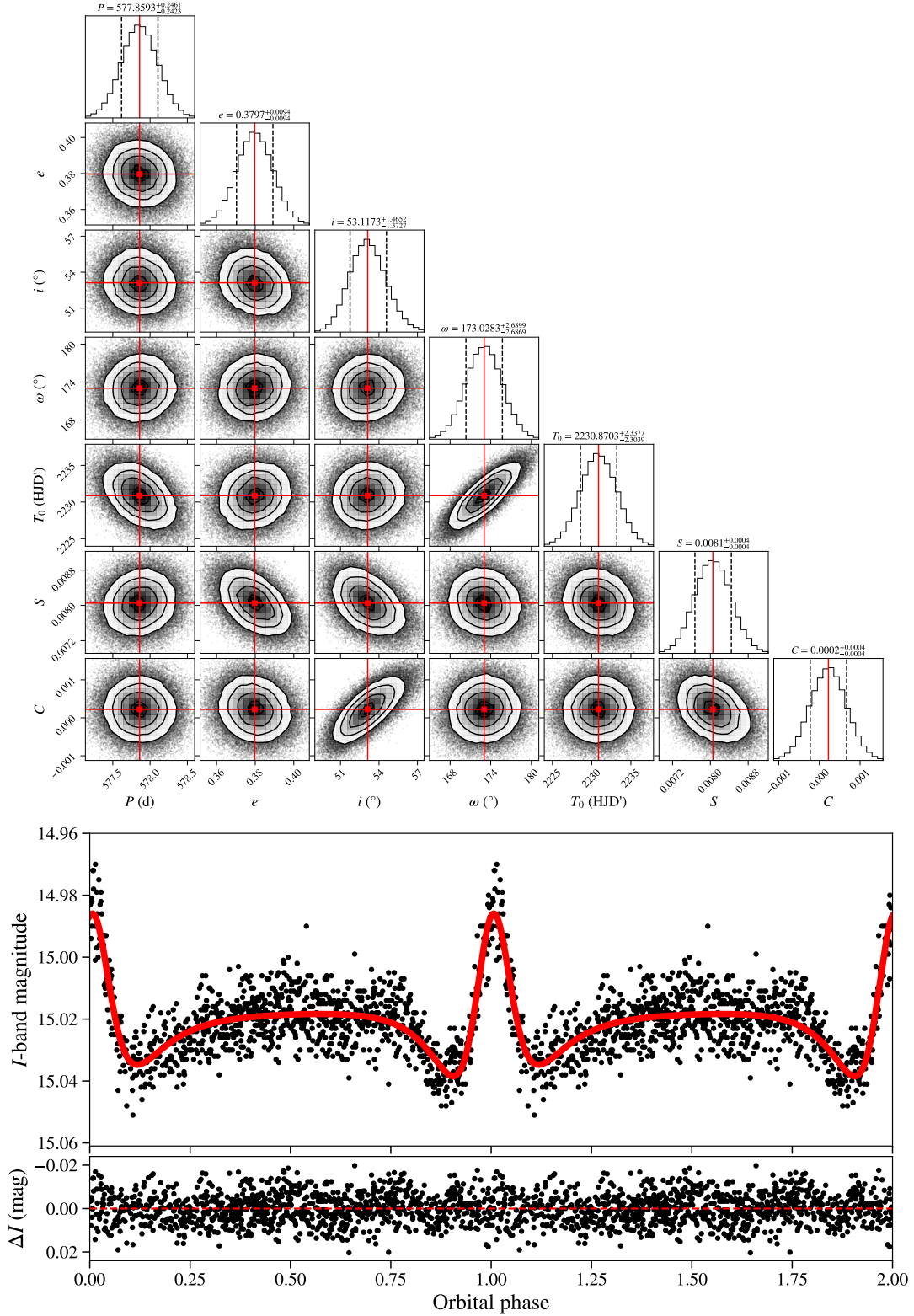


**Figure 2.** In the top panel, we present a corner plot with results of the MCMC fitting procedure for OGLE-LMC-HB-0018. Red lines indicate the median values of presented histograms for each parameter. Black dashed lines denote positions of 16th and 84th quantile. The  $T_0$  unit HJD' = HJD − 2,450,000. In the middle panel, we plot the Kumar's model (solid red line) fitted to the phase-folded light curve of OGLE-LMC-HB-0018 (black dots). The bottom panel shows the fitting residuals. The dashed red line denotes a zero-point.

obtained after the subtraction of the best-fitting Kumar’s model. The vast majority of the residual light curves reveal the presence of long-term variability that, regardless of whether it is physical or not, significantly enhances the signal in the frequency spectra at low frequencies. In order to get rid of these long-term brightness changes, prior to pre-whitening it was modeled with Akima cubic splines (Akima 1970) and subtracted from each residual light curve. After calculating the error-weighted Fourier frequency spectra, only peaks with the signal-to-noise ratio,  $S/N \geq 4$  were considered statistically significant. The mean noise level,  $N$  was derived as the mean signal of the frequency spectrum in the frequency range  $0-10 \text{ d}^{-1}$ . The final parameters characterizing the coherent variability were obtained by means of the error-weighted non-linear least-squares fitting of the truncated Fourier series to the corrected residual light curves. The formal errors of extracted frequencies as well as their amplitudes and phases were estimated using the covariance matrix.

The frequency  $f$  was considered a TEO if it was sufficiently close to the nearest harmonic of the orbital frequency, i.e. if the following condition was satisfied,  $|f/f_{\text{orb}} - n| \leq 3\sigma_{f/f_{\text{orb}}}$ . We estimated the error of  $f/f_{\text{orb}}$ ,  $\sigma_{f/f_{\text{orb}}}$  using a standard error-propagation formula  $\sigma_{f/f_{\text{orb}}} = (P^2\sigma_f^2 + f^2\sigma_P^2)^{1/2}$ , where  $\sigma_f$  and  $\sigma_P$  stand for the error of  $f$  and  $P$ , respectively. Recalling that TEOs can also have non-harmonic nature (provided that they formed via parametric instability NLMC channel), we examined if any sum of two non-resonant frequencies,  $f_1$  and  $f_2$  fulfill the inequality  $|(f_1 + f_2)/f_{\text{orb}} - n| \leq 3\sigma_{(f_1 + f_2)/f_{\text{orb}}}$ , where  $\sigma_{(f_1 + f_2)/f_{\text{orb}}}$  was calculated analogously to  $\sigma_{f/f_{\text{orb}}}$ . We did not look for the presence of non-harmonic TEOs resulting from higher order NLMC due to the insufficient precision of fitted frequencies.

## 5. DISCUSSION

### 5.1. Comparison of obtained $e$ , $i$ , $\omega$ parameters with previous works

To verify if the resulting parameters are consistent with true physical values, we have compared the solutions for the sample of our HBSs to the ones obtained using different methods, completely unrelated to the Kumar’s model.

For the comparison, we used results of the work by Nie et al. (2017). The authors studied 81 ellipsoidal RG binaries cataloged in the OCVS. In the modeling process, based on the 2010 version of the WD code, they used both light (mainly from the OGLE-II and OGLE-III) and radial velocity curves using data collected during their previous works (Nicholls et al. 2010, Nicholls &

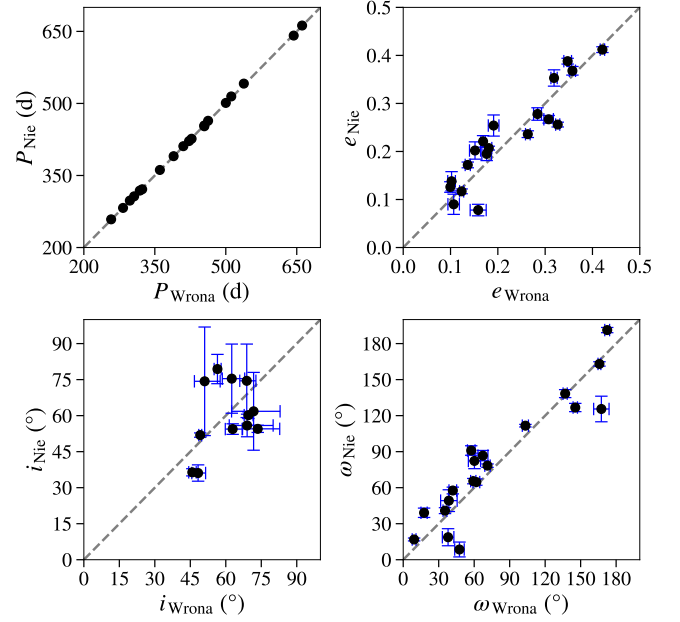


**Figure 3.** Comparison of the orbital parameters ( $P$ ,  $e$ ,  $i$ ,  $\omega$ ) obtained based on WD code (Nie et al. 2017, vertical axis) and using the Kumar’s model (this work, horizontal axis) for the overlapping sample of HBSs. The dashed gray line represents  $y = x$  line. We do not show error bars for  $P$  because their size are comparable to the plotted dots. The linear trends for  $P$ ,  $e$ , and  $\omega$  parameters are clearly visible, while for the inclination there is a significant scatter.

Wood 2012, Nie & Wood 2014). For the details of the modeling process using WD code, we refer the reader to Section 3 in the work of Nie et al. (2017). The total sample of 81 ellipsoidal variables consists of 59 systems with circular orbits and 22 with eccentric ones. Among the latter group, 19 stars were present in our catalog. The three remaining systems have a low eccentricity (0.069, 0.061, 0.054) and we have considered them as classical ellipsoidal variables.

The results of the comparison of the orbital parameters  $P$ ,  $e$ ,  $i$ ,  $\omega$  are presented in Figure 3. The horizontal and vertical axes represent values obtained during our analysis and the one presented by Nie et al. (2017), respectively. In the diagram containing inclination, we did not include stars with  $90^\circ$  flag from Nie et al. (2017) because it was assigned to the model when the WD code did not converge. Periods in both works are nearly identical. One can also see a very high correlation for the  $e$  and  $\omega$  values. Almost all pairs of points are consistent within the  $3\sigma$  region. This is also true for the  $i$  parameter, but contrary to  $e$  and  $\omega$  it does not show a clearly visible linear trend. This could be caused by the clumping of the  $i$  parameter in the  $50^\circ - 80^\circ$  range. Moreover, both methods – the WD code (as long as there are no



visible eclipses) and the MCMC fitting with the Kumar’s model, are weakly sensitive to the  $i$  parameter, when its value is larger than  $60^\circ$ .

Results shown in Figure 3, confirmed that the Kumar’s model is capable of finding reliable orbital parameters. In Section 5.5, we also discuss reliability of the Kumar’s model in the dependence on irradiation/reflection effect.

### 5.2. Distribution of the Kumar’s model parameters

In theory, the orientation of the binary system relative to the observer should be uniformly distributed, thus the inclination and the argument of the periastron should not favor any specific values. However, the observations of the HBSs seem to contradict this theory, which could be caused by the fact, that the amplitude of the brightness changes depends on the  $\omega$  and  $i$  parameters. Kumar et al. (1995) mentioned, that the amplitude of the light curve depends mainly on the mass and the structure of the star, although if we view a system from different angles, the contribution to the observed light curve from various modes are changed. For small  $i$  the main contribution to the light curve comes from the  $m = 0$  mode, while for higher  $i$  modes  $m = \pm 2$  start to dominate. The change of the contribution between modes mainly impacts the shape of the light curve, but it also affects the brightness. Thus if the observer sees only low-amplitude  $m = 0$  modes, the brightness changes could be too small for proper classification of the star.

Another factor that may skew the  $i$  and  $\omega$  distribution is the misclassification of stars based on the shape of the light curve. HBSs, especially with low inclinations, may mimic other types of variability, such as spotted stars (especially Ap type variables) or some kind of Be stars. On the other hand, for high  $i$  and for  $\omega$  near  $90^\circ$ , the light curve has a striking resemblance to the eclipsing binary (in the case of high eccentricity) or the classical ellipsoidal variable (for lower  $e$ ).

In the three panels of Figure 4, we present histograms of  $e$ ,  $i$  and  $\omega$ , respectively. Each chart shows a distribution of a given orbital parameter, separately for stars located toward the GB and MCs (colored lines) and combined (black lines). The HBS must have an eccentric orbit by definition and the higher the value of  $e$ , the easier way to distinguish HBS from a classical ellipsoidal variable, thus the low number of HBSs with  $e \lesssim 0.1$  is well understood. The lack of stars with high eccentricity is the result of a natural tendency of binaries to circularization of their orbit (e.g., Zahn 1975, Hut 1980). In the case of the histogram of  $i$ , the most prominent is the peak for  $i \approx 90^\circ$ . The most plausible, this is observational bias, caused by the fact that the majority

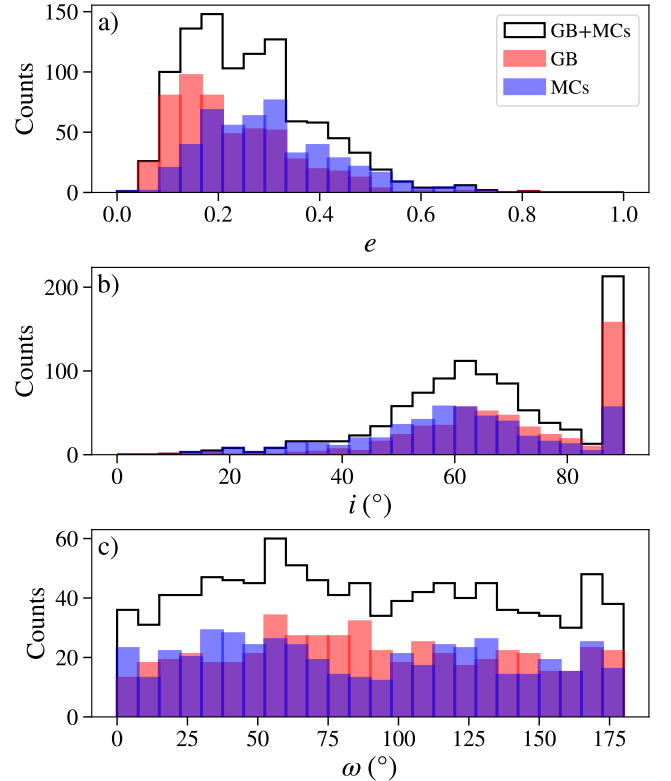


**Figure 4.** Histograms of orbital parameters for the sample of our HBSs located toward the GB (red boxes) and in the MCs (blue boxes). With the solid black line, we denote histogram of the combined samples of HBSs from all locations. In the panel a) we present histogram of the eccentricity,  $e$ , in the panel b) histogram of inclination,  $i$ , and in the panel c) histogram of the argument of the periastron,  $\omega$ .

of OGLE HBSs were found in the catalogs of eclipsing and ellipsoidal variables, which exhibit clear minima. In the histogram of the  $\omega$ , we have not noticed any specific features. The distribution of this parameter is nearly uniform.

### 5.3. Color-magnitude diagrams

The majority of the previously known HBSs have been found in the Kepler mission database, therefore those systems are mainly F, G, K class objects, located on the MS. There is also a group of systems containing hotter and usually more evolved stars of classes O, B, and A (e.g., Kołaczek-Szymański et al. 2021, and references therein). About 10% of the OGLE HBSs sample represent that group of stars.

On the other hand, about 90% of our HBSs belong to the red giant branch (RGB) or asymptotic giant branch (AGB), and less frequently to the horizontal branch. A large group of RG ellipsoidal variables were described by Soszyński et al. (2004). The majority of those systems have a circular orbit, but the authors also accentuated

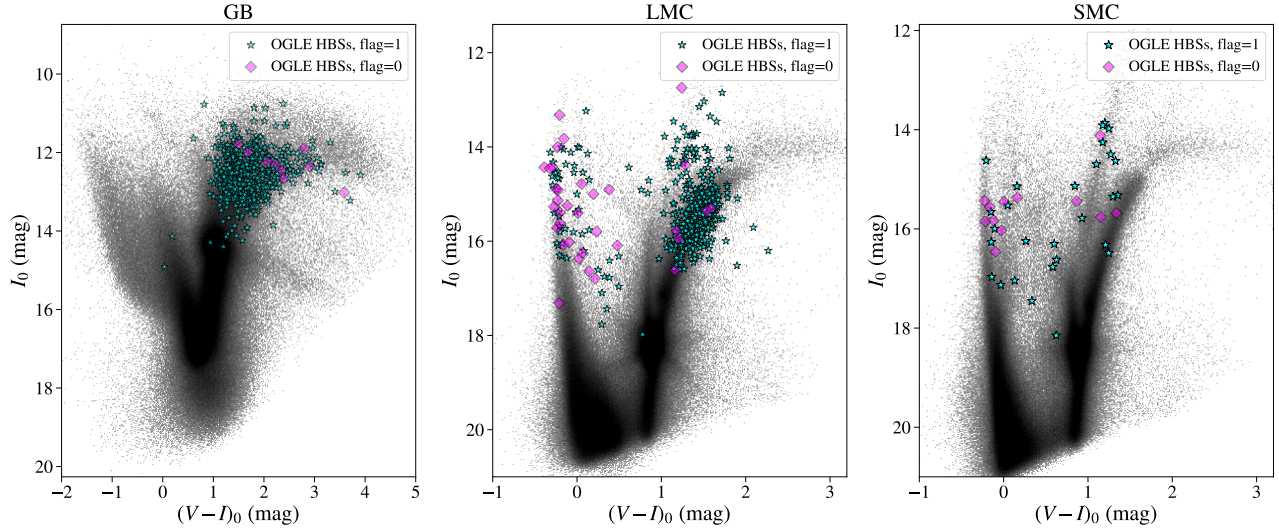


**Figure 5.** CMDs for the stars (gray points) located toward the GB (left panel), LMC (middle panel), SMC (right panel), and for the HBSs from the catalog (colored star symbols and diamonds). The CMDs have been created using calibrated photometric maps for several chosen OGLE-IV fields. The horizontal axis shows the de-reddened color index and the vertical axis is the mean magnitude with subtracted extinction. Star symbols (flag=1) represent HBSs with the well-fitted Kumar’s model, while diamonds (flag=0) denote stars without a proper model (mainly systems showing deep eclipses). We can see that the majority of the HBSs from the GB and LMC lie on the RGB or AGB. In the LMC, we can also see a large group of stars located on the blue part of the MS.

a group of systems with high eccentric orbits. Until our work, presented in Wrona et al. (2021), they were the largest collection of RG HBSs (officially cataloged as ellipsoidal variables).

#### 5.3.1. Color-magnitude diagram for the GB

The sample of our HBSs located toward the GB is dominated by stars lying on the RGB and AGB, which is noticeable in the color-magnitude diagram (CMD) in the left panel of Figure 5. Background for the CMD has been created based on calibrated photometric maps for several OGLE-IV fields located around the Galactic center. The  $I$ -band extinction values  $A_I$  and color excess of stars  $E(V-I)$  were determined using extinction maps presented by Nataf et al. (2013). Extinction toward the GB is very heterogeneous what causes a blur of stars on the CMD, which is clearly visible on the red clump (RC, a wide group of points around  $[(V-I)_0, I_0] = [1.05, 14.3]$ ). If there was no extinction, most of HBSs from our collection would be saturated, because the brightness limit for the Warsaw telescope is about 13 mag in the  $I$ -band. There are only 2 systems on the MS. Such a small number of HBSs in this region was very unexpected because most of the HBSs known before were in this place on the CMD. The absence of such HBSs in our catalog is probably the result of the data selection.

#### 5.3.2. Color-magnitude diagram for the MCs

In the middle and right panels of Figure 5, we present positions of the HBSs sample on the CMDs in the Large Magellanic Cloud (LMC) and in the Small Magellanic Cloud (SMC), respectively. Both CMDs have been created similarly to the CMD for GB. We took calibrated photometric maps for several OGLE-IV fields and we combined them creating the background for the HBSs sample. The  $E(V-I)$  color excess was calculated using the reddening map of the MCs (Skowron et al. 2021).

In contrary to the distribution of HBSs on the CMD for the GB, here we can easily distinguish at least two large groups of HBSs. The first one consists of hot MS and Hertzsprung-gap stars of spectral type from late O to F, which is consistent with HBSs from the Kepler sample. The second noticeable group (especially for the LMC) is located on the RGB and AGB, which is in agreement with the results for the GB. There are also less numerous groups, e.g., one HBS near RC for each location and a few stars on the horizontal branch.

#### 5.4. Evolutionary status of the OGLE HBSs

For a better picture of the evolutionary status of the OGLE HBSs, we describe them in the two following subsections. The first one refers to the stars located on or near to the MS and in the latter one, we discuss systems containing an RG star. Here we analyze only stars located in the LMC. The SMC sample is too small for such an analysis. In the GB, extinction is highly non-uniformly distributed, which hampers precise determi-

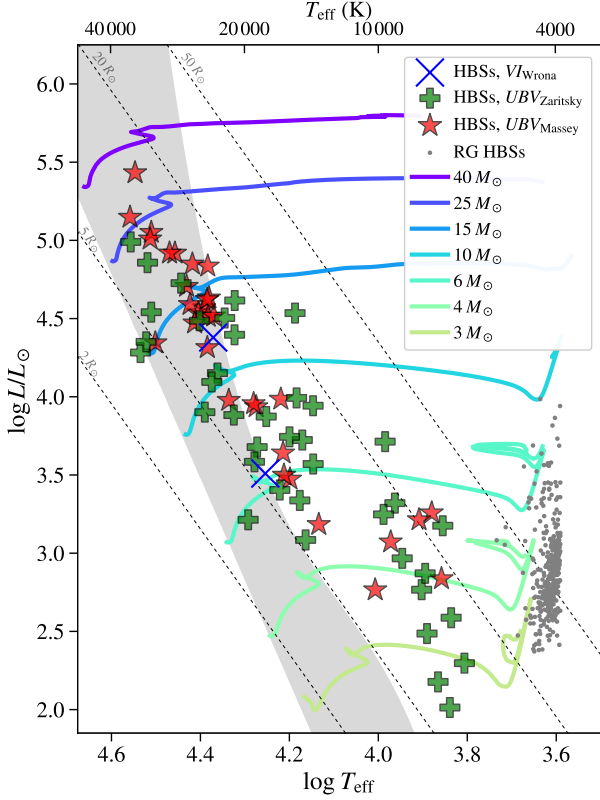


**Figure 6.** HR diagram for the LMC subsample of the OGLE HBSs located on or near to the MS (shaded area). We calculated effective temperatures using  $(U-B)$  and  $(B-V)$  photometric colors provided by Massey (2002) – green pluses or by Zaritsky et al. (2004) – red stars. We did not find  $UBV$  data for two of HBSs and we assessed their temperatures based on  $(V-I)$  color – blue crosses. We derived luminosities of HBSs from distance modulus using de-reddened  $I$ -band mean magnitude and  $B_I$  bolometric correction. Colored solid lines denote evolutionary tracks generated by MIST v1.2 for masses in range  $3-40 M_\odot$ . We used constant value of metallicity  $[\text{Fe}/\text{H}] = -0.4$  dex and initial-to-critical rotational velocity ratio  $v/v_{\text{crit}} = 0.4$ . We show evolution tracks only to the He-core-burning phase. Dashed black lines show lines of constant radius from 2 to  $50 R_\odot$ .

nation of the color and, in turn, resulting in very high uncertainties in the effective temperature of stars. Moreover, for the LMC we can assume that all stars are located at the same distance (the distances between stars are insignificant compared to the distance to the LMC), which allows us to determine an absolute magnitude for each star. In the GB, we do not know the distance for the majority of stars, thus we are not able to calculate precise absolute magnitudes.

#### 5.4.1. HBSs with an MS or Hertzsprung-gap primary

The HBSs containing a hot star ( $T_{\text{eff}} \gtrsim 8000$  K) are located mainly on the MS or near to the MS (perhaps

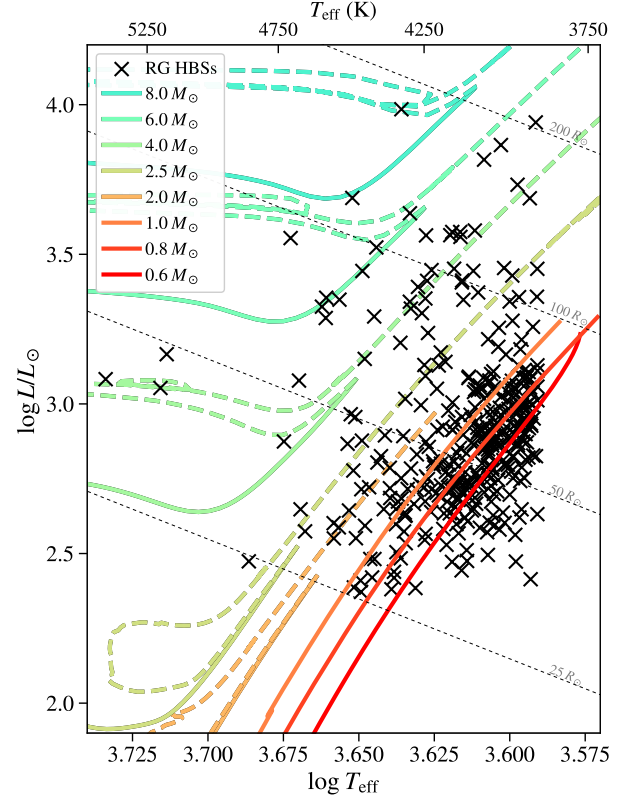


**Figure 7.** HR diagram for the LMC subsample of the OGLE HBSs with an RG star (black crosses). We calculated effective temperatures based on  $(V-I)$  color and color-temperature relation presented by Houdashelt et al. (2000). Colored solid and dashed lines present evolutionary tracks generated by MIST v1.2 for masses in range  $0.8-8.0 M_\odot$ . For the masses below or equal  $1 M_\odot$ , we show an evolution track only to the RGB tip (solid line). For higher masses, we also plot evolution after this phase (dashed line). We adapted metallicity gradient from  $[\text{Fe}/\text{H}] = -1.0$  dex, for low-mass systems, to the  $[\text{Fe}/\text{H}] = -0.5$  dex, for the highest masses. We also used initial-to-critical rotational velocity ratio  $v/v_{\text{crit}} = 0.0$ . Thin dashed black lines show lines of constant radius from 25 to  $200 R_\odot$ .

Hertzsprung gap). HBSs with cooler MS stars usually show very small brightness changes (less than a few thousandths of magnitude, e.g., Kirk et al. 2016) what makes them very difficult to identify in the OGLE data.

In Figure 6, we present the Hertzsprung-Russell (HR) diagram for the bluest part of our HBSs located in the LMC. To calculate effective temperatures of stars, we used  $UBV$  photometry obtained by Massey (2002) and Zaritsky et al. (2004). We followed the prescription de-

scribed in Massey et al. (1989):

$$\log T_{\text{eff}} = \begin{cases} 3.994 - 0.267Q + 0.364Q^2, & \text{if } (B - V)_0 < 0.0; \\ 3.990 - 0.510(B - V)_0, & \text{if } 0.0 < (B - V)_0 < 0.2; \\ 3.960 - 0.344(B - V)_0, & \text{if } 0.2 < (B - V)_0 < 0.5, \end{cases} \quad (9)$$

where  $Q = (U - B) - 0.72(B - V)$  is the reddening-free index and  $(B - V)_0 = (B - V) - E(B - V)$  is the dereddened color. The color excess  $E(B - V)$  is calculated from  $E(V - I)$  using  $E(B - V) = E(V - I)/1.318$ .

For two stars, the  $UBV$  photometry was unavailable. In order to estimate photometric temperatures for these stars, we used  $T_{\text{eff}} - (V - I)_0$  grid collected in the work of Bessell et al. (1998) for early-type stars (their Table 1) and for the surface gravity  $\log g = 4.5$ .

To calculate the bolometric luminosity, we used a simple Pogson's equation:

$$\log L/L_{\odot} = -0.4(M_{\text{bol}} - M_{\text{bol},\odot}), \quad (10)$$

where  $M_{\text{bol}} = M_I + BC_I$  and  $M_{\text{bol},\odot} = 4.74$  mag (Prša et al. 2016a) are the bolometric absolute magnitudes of a star and the Sun, respectively. Assuming the distance to the LMC as  $d_{\text{LMC}} = 49.59$  kpc (Pietrzyński et al. 2019) and calculating the bolometric correction,  $BC_I$  for  $I$  filter, we find  $M_{\text{bol}}$  as:

$$M_{\text{bol}} = I_0 - 5 \log d_{\text{LMC}} + 5 + BC_I. \quad (11)$$

$I_0$  is the mean  $I$ -band magnitude with subtracted extinction. We computed  $BC_I$  values based on Bolometric Correction Tables available on the MIST project website<sup>4</sup>. We assumed a metallicity  $[\text{Fe}/\text{H}] = -0.5$  and  $\log g = 4.5$ .

In Figure 6, with colored solid lines, we marked the MIST v1.2 evolutionary tracks by Choi et al. (2016) and Dotter (2016), computed with the Modules for Experiments in Stellar Astrophysics (MESA) code (e.g., Paxton et al. 2011, 2013). For all tracks we set initial rotation of  $v/v_{\text{crit}} = 0.4$  and metallicity  $[\text{Fe}/\text{H}] = -0.4$  (e.g., Harris & Zaritsky 2009).

When comparing positions of the HBSs to the evolutionary tracks, we see a wide range of possible zero-age main-sequence (ZAMS) masses of systems, from about  $3M_{\odot}$  to as high as  $40M_{\odot}$ .

There is also a noticeable trend – the cooler and less luminous the star, the farther it lies from the MS

(marked as shaded area in Figure 6). The second notable observation is that the HBSs form a group along the line which is parallel to the line of constant radius. Moreover, we can see that the majority of HBSs lie in the channel between 5 and  $20 R_{\odot}$ .

There are at least two possible explanations for the observed departure of less luminous OGLE HBSs from the MS. The first one is an observational bias caused by the dependence between the stellar radius and the amplitude of the heartbeat. In theory, the larger the stellar radius, the larger the tidal deformation of stellar surface, thus the larger the amplitude of brightness changes. Stars with  $M_{\text{ZAMS}} < 10M_{\odot}$  begin their evolution on the MS with the radius not exceeding  $4\text{--}5 R_{\odot}$ , thus the heartbeat amplitudes may be too low for detection in ground-based surveys like the OGLE.

The second explanation is the increasing light contamination from the companion for less luminous primaries, which may cause a shift in the location on the HR diagram. If we assume a system where the primary and companion stars have similar effective temperatures, the location of this system on the HR diagram will be shifted upward relative to the position occupied by the primary itself. On the other hand, if the companion has a lower effective temperature, the position of the entire system on the HR diagram will be shifted to the right relative to the position of the primary. In Figures 6 and 7, the markers show the location of the primaries with the assumption that the light contamination from the companion is negligible, which may not be correct. This is probably the case for about half of hot HBSs because they are also eclipsing binaries with clearly visible primary and secondary eclipses. To determine the amount of contamination from the companion, further analysis is necessary, especially with the use of spectroscopic observations, which would allow for a more accurate estimation of the effective temperature of the main component. However, such an analysis is beyond the scope of this work.

#### 5.4.2. HBSs with an RG primary

The most numerous group of the OGLE HBSs is located in the RG part of the HR diagram. Those systems generally consist of a low-mass ( $M_{\text{ZAMS}} \lesssim 2M_{\odot}$ ) or intermediate-mass ( $2M_{\odot} \lesssim M_{\text{ZAMS}} \lesssim 8M_{\odot}$ ) primary, which is evolving through the RGs region, and a lighter companion, which most likely belongs to the MS.

Unlike the HR diagram for the hot stars described in the previous subsection, here we decided to obtain photometric temperatures based on the  $(V - I)_0$  color, derived directly from the OGLE data. We used an empirical relation from Houdashelt et al. (2000) for giant

<sup>4</sup> <http://waps.cfa.harvard.edu/MIST/index.html>



stars:

$$T_{\text{eff}} = 8556.22 - 5235.57 \cdot (V - I)_0 + 1471.09 \cdot (V - I)_0^2, \quad (12)$$

which is reliable for a range  $0.70 < (V - I)_0 < 1.68$ . Bolometric luminosities were calculated using Equations (10) and (11). We utilized the bolometric correction from YBC database<sup>5</sup>, described by Chen et al. (2019).

In Figure 7, we present the HR diagram for the RG part of the HBSs located in the LMC. Similarly to the blue part of the HBSs, here we also generated MIST evolutionary tracks. Solid lines represent stellar evolution until the RGB tip phase and dashed lines show the subsequent stages (shown only for masses  $M_{\text{ZAMS}} > 1M_{\odot}$ ), until the AGB tip. We used metallicity gradient depending on the initial mass (e.g., Harris & Zaritsky 2009):

$$[\text{Fe}/\text{H}] = \begin{cases} -1, & \text{if } M_{\text{ZAMS}} \leq 1.0M_{\odot}; \\ -0.6, & \text{if } 1.0M_{\odot} < M_{\text{ZAMS}} \leq 2.5M_{\odot}; \\ -0.5, & \text{if } 2.5M_{\odot} < M_{\text{ZAMS}}. \end{cases} \quad (13)$$

For each track we set initial rotation  $v/v_{\text{crit}} = 0.0$ .

The obtained HR diagram is fully consistent with the one presented in Figure 4 of Nie et al. (2017), even though we used a slightly different approach to construct it. Those authors used an evolutionary track from Bertelli et al. (2008),  $\log L/L_{\odot}$  and  $T_{\text{eff}}$  parameters were obtained based on  $I$  and  $K$  photometry using the prescription from Nie et al. (2012), and last but not least, their HR diagram refers mainly to the classical ellipsoidal variables (only 22 systems have an eccentric orbit), while our sample includes only HBSs. In both works, the largest part of stars occupy the region for initial masses of less than  $1.85\text{--}2M_{\odot}$ , which indicates that these systems contain the RG star which is evolving through the RGB (with degenerate He core) or, in the case of stars more massive than the Sun, on the AGB (with degenerate C/O core).

There is also a second group of HBSs, which is represented by stars with a larger initial mass. These stars can be in any medium-stage of their "life", from evolving on the RGB with a non-degenerate He core, through the He-core-burning phase, to the evolution on the AGB. For stars with  $T_{\text{eff}} \lesssim 4250$  K ( $\log T_{\text{eff}} \lesssim 3.63$ ) more favored is an option with AGB evolution because the tip of the RGB and He-core-burning phase for stars with  $M_{\text{ZAMS}} \lesssim 6M_{\odot}$  do not exceed such temperature.

### 5.5. The impact of irradiation/reflection effect

In order to quantitatively estimate the impact of irradiation/reflection effect on the shape of the OGLE  $I$ -band light curves of HBSs located in the LMC, we run a set of dedicated simulations. We used PHOEBE 2 modeling software (version 2.3; Prša et al. 2016b, Horvat et al. 2018, Jones et al. 2020, Conroy et al. 2020) for this purpose and performed two groups of simulations. The first one refers to HBSs with the primary component being an RG. The majority of our HBSs fall into this group. In the second group, we considered HBSs with a massive primary component located on the MS or passing through the Hertzsprung gap. We will refer to these two groups of simulations as "S-RG" and "S-MS", respectively.

The S-RG simulations were done as follows. We considered three masses of RGs being a primary component, 1, 2 and  $6M_{\odot}$  with the corresponding radii of 50, 75 and  $100R_{\odot}$  (cf. Figure 7). For each mass of the primary component we generated 10 000 binaries with mass ratios  $q$ ,  $e$ ,  $i$ ,  $\omega$ , and periastron distances relative to sum of radii of components  $r_{\text{peri}}/(R_1 + R_2)$  drawn from uniform distributions  $\mathcal{U}_{[\alpha, \beta]}$  on the interval  $[\alpha, \beta]$ . We comment on them below.

- $q \sim \mathcal{U}_{[0.2, 0.9]}$  – We did not consider  $q > 0.9$  because we realistically assumed that the secondary companions are MS stars.  $q \approx 1$  would suggest that secondary is also an RG, which in turn would result in very long orbital periods, unobserved by us. On the other hand, the overall strength of tides is proportional to  $q$ , therefore we omitted systems with  $q < 0.2$ . The typical peak-to-peak amplitude of heartbeat in our sample of RGs is relatively high,  $\sim 0.05$  mag, hence it rather excludes the possibility of low- $q$  companions.
- $e \sim \mathcal{U}_{[0.15, 0.70]}$  – We adopted a representative range of eccentricities observed in the analyzed collection of OGLE HBSs.
- $i \sim \mathcal{U}_{[0, \pi/2]}$ ,  $\omega \sim \mathcal{U}_{[0, 2\pi]}$  – Any possible values of  $i$  and  $\omega$  were allowed in the simulation.
- $r_{\text{peri}}/(R_1 + R_2) \sim \mathcal{U}_{[1, 4]}$  – The strength of tidal forces at periastron falls off rapidly as  $r_{\text{peri}}^{-3}$ . Therefore, we set a maximum limit of  $r_{\text{peri}}/(R_1 + R_2)$  to 4 in order to simulate only the orbits with a chance to reproduce detectable heartbeat signals.

The values of  $q$ ,  $i$ ,  $\omega$  and  $r_{\text{peri}}/(R_1 + R_2)$  were generated independently from each other. The drawn values of  $r_{\text{peri}}/(R_1 + R_2)$  were subsequently transformed to orbital periods,  $P$  using Kepler's third law. During simulations, only these systems were accepted that did not

<sup>5</sup> <http://stev.oapd.inaf.it/YBC/>

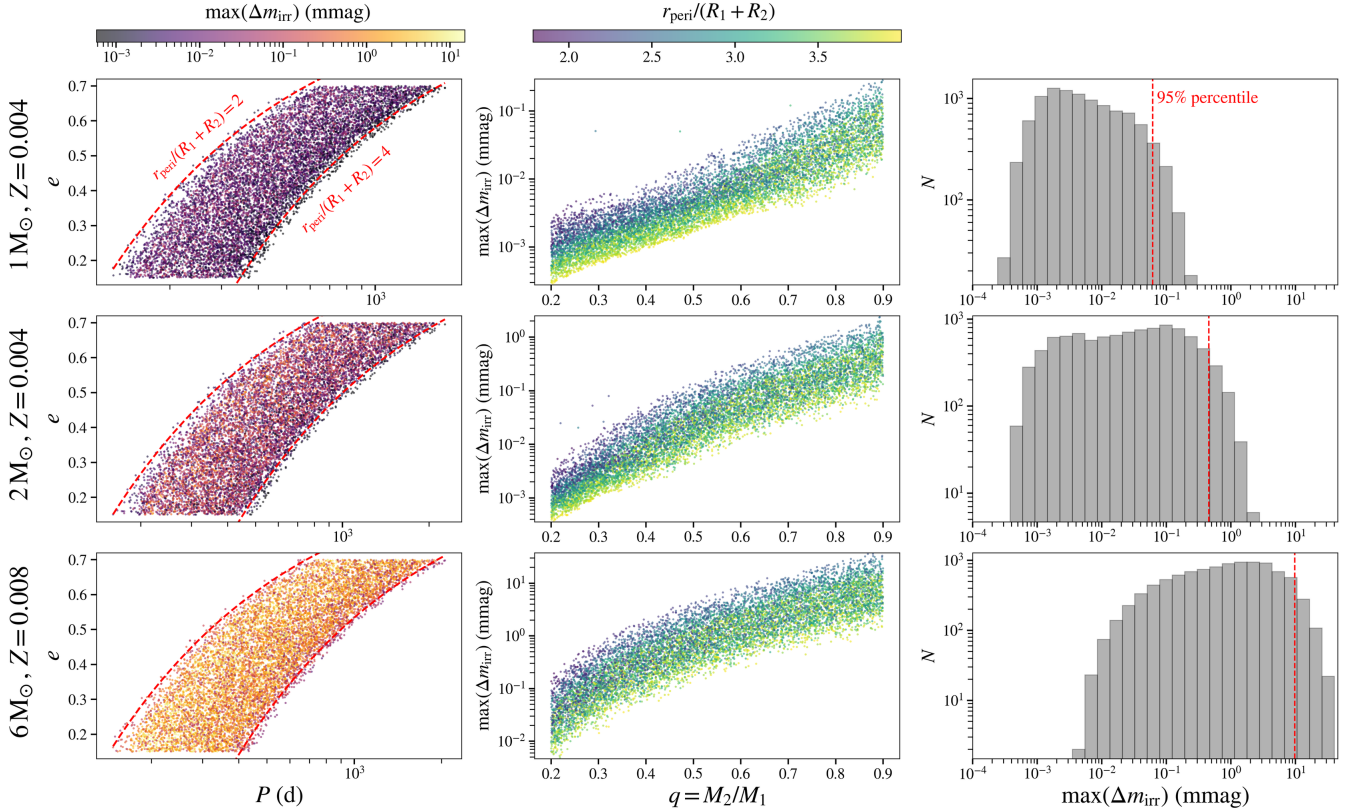


**Figure 8.** Results of the S-RG simulations for three different masses of RG primary component,  $1 M_{\odot}$  (top row),  $2 M_{\odot}$  (middle row) and  $6 M_{\odot}$  (bottom row). (Left column): The orbital period-eccentricity distributions of simulated binaries. The maximum contribution of the irradiation/reflection effect in the  $I_C$  passband,  $\max(\Delta m_{\text{irr}})$  is color-coded. The dashed red lines denote systems with  $q = 0.5$  and  $r_{\text{peri}}/(R_1 + R_2) = 2$  or  $4$ ; (Middle column): The distributions of simulated binaries on the  $q$ - $\max(\Delta m_{\text{irr}})$  plane. The periastron distance scaled by the sum of radii of the components is color-coded; (Right column): The histograms of simulated  $\max(\Delta m_{\text{irr}})$  values. The vertical dashed red lines indicate the position of 95% percentile; See more details in the text.

overflow at the periastron, i.e. the detached geometry is always preserved. The remaining physical parameters of the components, namely their effective temperatures and the radii of secondaries, were taken from the MIST isochrones of the age compatible with the parameters of the primary RG star. We assumed  $[\text{Fe}/\text{H}] = -0.7$  for systems with  $1$  and  $2 M_{\odot}$  primaries while for  $6 M_{\odot}$  we adopted a higher value of  $-0.4$  in order to account for the metallicity gradient observed in the LMC. The bolometric albedos were set to  $0.6$  and  $1.0$  for components with convective and radiative envelopes, respectively. The surfaces of both components were simulated within PHOEBE 2 with 4000 triangular elements. The radiative properties of stars with effective temperatures above  $4000$  K were obtained from ATLAS9 model atmospheres (Castelli & Kurucz 2003). Otherwise, the PHOENIX models (Hauschildt et al. 1997, Husser et al. 2013) were used for cooler components. Both grids of model atmospheres are incorporated into PHOEBE 2 with the accompanying limb darkening tables. Finally, for every single system, two  $I_C$ -band light curves were calculated.

One with the irradiation/reflection effect being switched off and the second one with the aforementioned effect treated in the formalism developed by Wilson (1990). Next, we were searching for the largest difference between these two synthetic light curves, which we denote as  $\max(\Delta m_{\text{irr}})$ .

Figure 8 summarizes the effects of S-RG simulations. The first thing that draws attention is the clear correlation between  $q$ ,  $r_{\text{peri}}$  and  $\max(\Delta m_{\text{irr}})$  (second column in Figure 8). The larger  $q$  and lower  $r_{\text{peri}}$ , the more pronounced impact of the irradiation/reflection effect. Nevertheless, for systems with the primary's mass  $\lesssim 2 M_{\odot}$  the  $\max(\Delta m_{\text{irr}}) \lesssim 1$  mmag. This fact allows us to state that the Kumar's model should return trustworthy orbital parameters for the majority of the OGLE HBSs containing an RG. This is because most of them are low-mass stars, as indicated by their positions on the HR diagram (Figure 7). The situation is different for massive RGs, companions of which may have high effective temperatures and luminosities, hence the irradiation/reflection effect is significant. In such a sce-

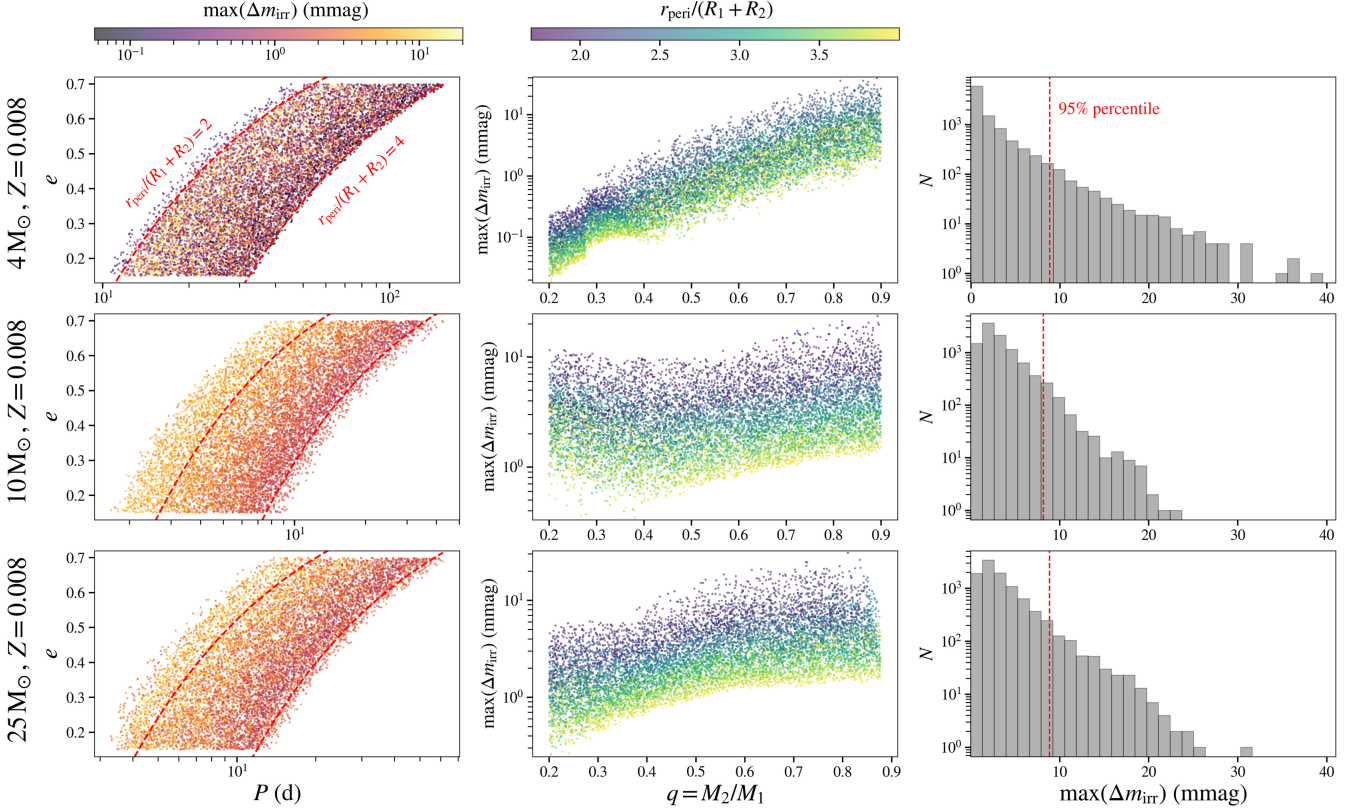


**Figure 9.** The same as Figure 8 but for the S-MS set of simulations.

nario, the 95% percentile of  $\max(\Delta m_{\text{irr}})$  is equal to circa 10 mmag, but systems with  $\max(\Delta m_{\text{irr}})$  up to 40 mmag can occur. Depending on the amplitude of the heartbeat observed in HBSs that contain the massive RG, one should be aware that the irradiation/reflection effect may become comparable to the ellipsoidal variability. Therefore, the orbital parameters obtained for such systems via fitting the Kumar’s model to their light curves should be treated rather as estimates.

The simulations S-MS were performed analogously to the S-RG, but here we considered different masses of primary components, 4, 10, and  $25 M_{\odot}$  (cf. Figure 6). To realistically reflect the evolutionary phase of these components visible in Figure 6, we assumed  $4 M_{\odot}$  primary to be in the middle of its Hertzsprung gap while 10 and  $25 M_{\odot}$  primaries located halfway between ZAMS and terminal-age main-sequence (TAMS). All models were assumed to have  $[\text{Fe}/\text{H}] = -0.4$ . The rest of the parameters and methods necessary to run S-MS simulations were identical to the S-RG set-up described above.

Similarly to Figure 8, Figure 9 shows the results of S-MS simulations run. We found that for massive HBSs which are still on the MS or near it, the irradiation/reflection effect in the  $I_C$ -band is generally non-negligible. The 95% percentile of  $\max(\Delta m_{\text{irr}})$  is equal to around 9 mmag for all variants in this simulations.

However, still numerous systems can have an amplitude of the irradiation/reflection effect in the range of 10–30 mmag. Considering these facts, we would like to emphasize that orbital parameters derived by us for massive MS HBSs may deviate from actual values and should be treated with caution.

Although the above analysis was performed for HBSs located in the LMC, its results should also remain valid for systems from the SMC and GB. The irradiation/reflection effect will mainly affect the estimation of the inclination and argument of the periastron as it fills the “dips” in the heartbeat signal. On the other hand, the obtained values of eccentricity should always be close to the actual state. The eccentricity is determined by the width of the heartbeat pulse, which is not significantly affected by the irradiation/reflection effect.

### 5.6. Period–amplitude diagrams

The orbital period and  $I$ -band amplitude distributions for the GB sample of HBSs are presented in the top panel of Figure 10. Our sample, contrary to HBSs from the Kepler data, mainly consists of systems with a long orbital period (mostly a few hundred days) and with high amplitude brightness variations as for the HBS (a few hundredths of a magnitude and larger). The color scale reflects the effective temperatures of the stars, based

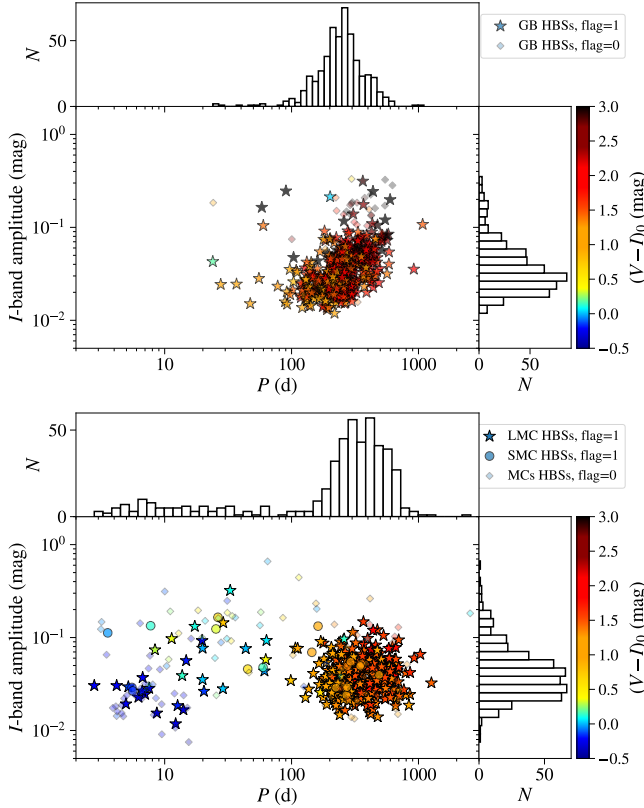


**Figure 10.** Period-amplitude diagrams and histograms for the HBSs sample from our collection for the GB (top panel) and MCs (lower panel). Flags have the same meaning as in Figure 5. The color of the markers represents the de-reddened color value which corresponds to the effective temperature of the star surface. The orbital period for most HBSs is of an order of a few hundred days while the  $I$ -band amplitude is about a few hundredths of a magnitude. In the lower panel, one can see the trend in data – the lower the orbital period, the hotter (bluer) the star.

on the de-reddened  $(V - I)_0$  color index. Black color ( $(V - I)_0 > 3.0$ ) is a mark for stars located in the regions not included in the extinction maps.

In the lower panel of Figure 10, we show a similar diagram for HBSs from the LMC (marked as stars) and SMC (circles). The period and amplitude ranges for the cooler group of HBSs (yellow and red colors, types from G to M) are similar to the ranges for the sample from the GB, which indicates the common nature of those systems. Hot stars (blue and cyan colors, types from late O to F), which correspond to HBSs sample located on the MS or its vicinity, have a similar mean value of the amplitude, but slightly bigger scatter. However, the orbital period distribution for hotter stars is extremely different. Those systems have much shorter periods, from a few days to several tens of days. It is the result of different sizes of the primaries. In Figures 6 and 7, we can see

that the HBSs located on the blue part of the HR diagram reach sizes from 5 to  $25 R_\odot$ , while the HBSs from the red part of the HR diagram have radii from 25 to even  $200 R_\odot$ . Since stars in the system cannot come too close to each other, the smaller the stars, the smaller the minimum distance is needed, thus the shorter the orbital periods. In Figure 10, we can also see a trend in the period–color relations, the higher the value of color, the longer the orbital period in the system.

### 5.7. Period–luminosity relations for RG HBSs

RG variable stars, such as Miras, OGLE Small Amplitude Red Giants (OSARGs), semiregular variables (SRVs), Long Secondary Periods (LSPs), or long-period eclipsing and ellipsoidal stars exhibit classical period–luminosity relations. Within each of those classes, in the period–luminosity (PL) diagram, the stars assemble into linear sequences, marked with letters from A do E (e.g., Wood et al. 1999, Soszyński et al. 2004). The sequences differ in slope, spread and they are also shifted relative to each other. These parameters also depend on the set of filters which were used (e.g., scatter is much smaller for NIR filters than for optical ones). In the case of HBSs, the crucial is sequence E which is formed by eclipsing and ellipsoidal variables.

In Figure 11, we present PL diagrams for RG variables from the OCVS (references are listed in Table 1), including HBSs from our collection. We plotted PL diagrams separately for the LMC and GB, using two types of the extinction-free Wesenheit indices  $W_I$  and  $W_{JK}$ , defined as:

$$W_I = I - R_{I,V} \cdot (V - I); \quad (14)$$

$$W_{JK} = K_s - R_{K_s,J} \cdot (J - K_s), \quad (15)$$

where  $R_{I,V} = A_I/E(V - I)$  and  $R_{K_s,J} = A_{K_s}/E(J - K_s)$  are the total-to-selective extinction. We adopted  $R_{I,V} = 1.14$ ,  $R_{K_s,J} = 0.67$  for the GB sample (e.g., Dutra et al. 2002, Pietrukowicz et al. 2015) and  $R_{I,V} = 1.55$ ,  $R_{K_s,J} = 0.686$  for the LMC sample (e.g., Soszyński et al. 2009, Storm et al. 2011). We do not show PL diagrams for objects located in the SMC, because of low number of RG HBSs.

All  $I$ - and  $V$ -band data come from the OGLE survey. In the case of MCs, values for  $J$ - and  $K_s$ -band have been taken mainly from IRSF and additionally from 2MASS, and in the case of the GB, we have taken into account only data from the latter survey.

In all PL diagrams, we notice a linear trend formed by HBSs – the longer the orbital period, the more luminous the system. The second notable aspect is that HBSs seem to stick to the long period ( $\log P \gtrsim 2$ ) group of



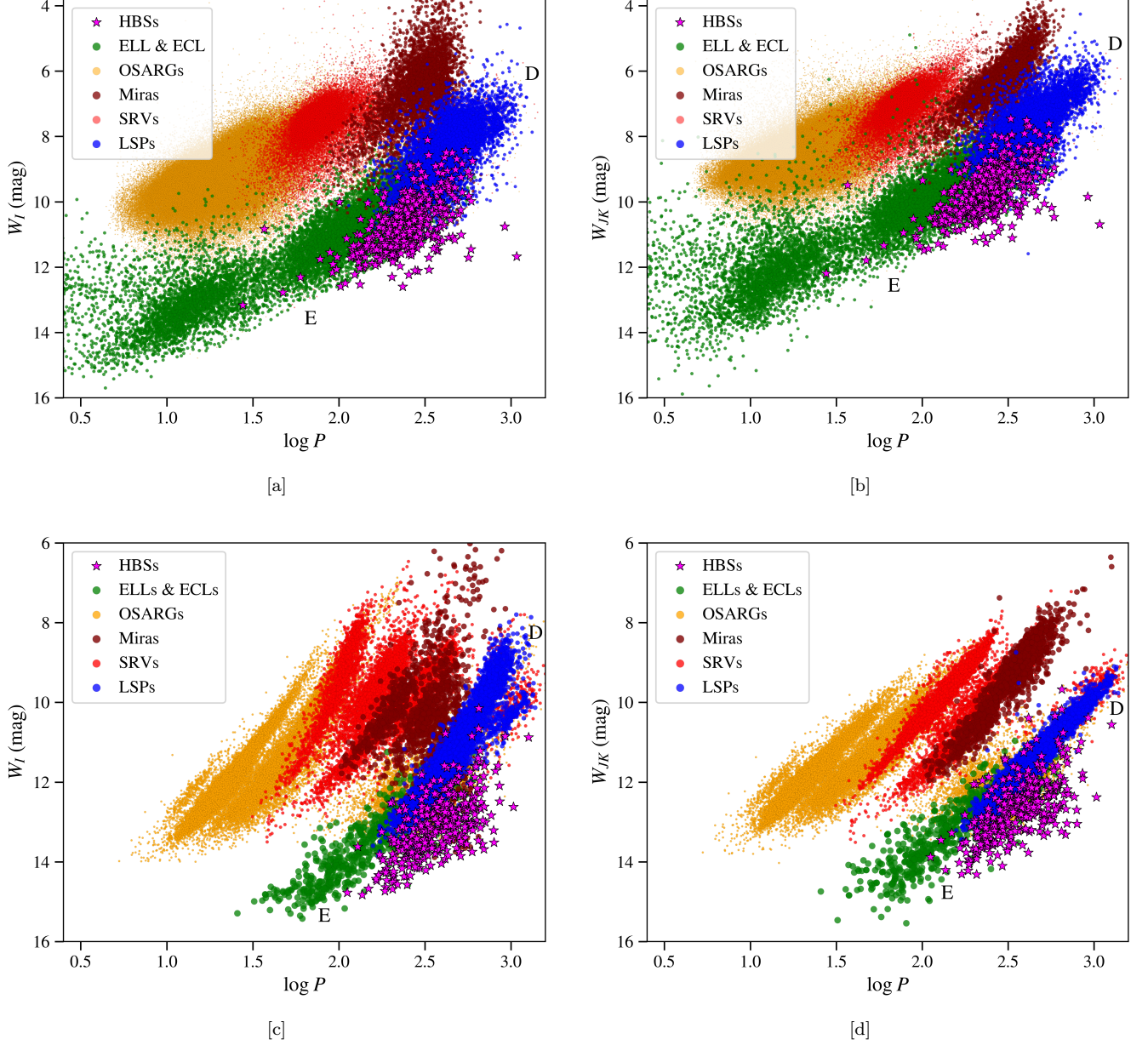


**Figure 11.** PL diagrams for Long Period Variables (yellow, brown, pink, and red points), ellipsoidal and eclipsing binaries (green points), and HBSs (magenta stars), located toward the GB (panels [a] and [b]) and LMC (panels [c] and [d]). On the left-hand side, luminosities are shown in the  $W_I$  Weisenheit index and on the other side in  $W_{JK}$ . Note that despite the location and Weisenheit index, HBSs are a prolongation of the ELL & ECL group (known as sequence E) and LSPs (known as sequence D) toward longer periods.

eclipsing and ellipsoidal variables, but also to the LSP stars (sequences E and D). This feature was also noticed by [Soszyński et al. \(2004\)](#) and highlighted by [Nie et al. \(2017\)](#). However, those analyzes involved only a small group of HBSs located in the LMC. Here we show that those remarks are genuine for a larger sample of HBSs in the LMC as well as for HBSs located toward the GB.

Recently, [Soszyński et al. \(2021\)](#) showed that LSP variables (sequence D) are systems that contain an RG

and a stellar or sub-stellar companion. In combination with eclipsing and ellipsoidal stars (sequence E), they form a group with a wide range of periods (from a few days to about three years), for which the brightness changes are driven mainly by the interactions between the components of the binary system. Since the RG part of the HBSs form a group in the similar region of the PL diagram (sequences D and E), thus it is likely that they are binary systems as well.

**Table 1.** References to the catalog papers of used Long Period Variables.

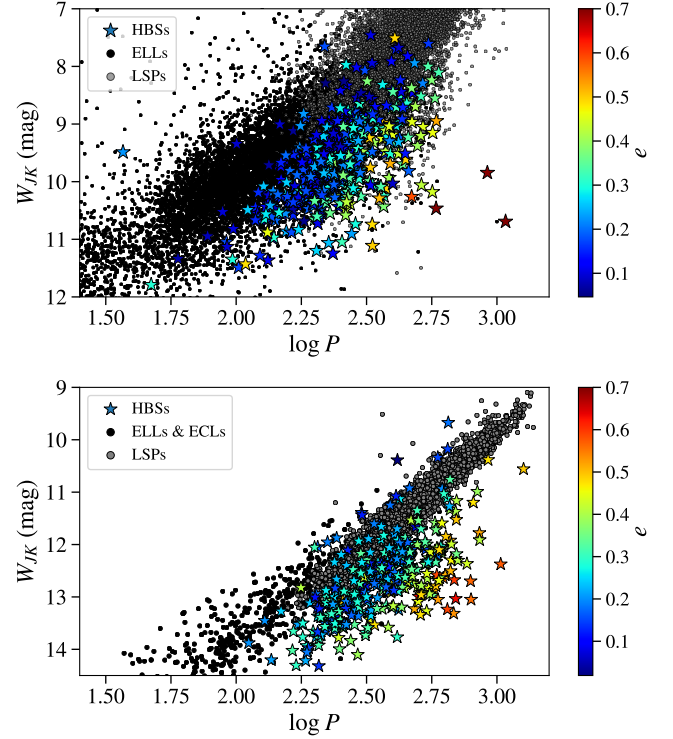
Location	Variability class	Reference
LMC	OSARG	Soszyński et al. (2009)
LMC	Mira	Soszyński et al. (2009)
LMC	SRV	Soszyński et al. (2009)
LMC	LSP	Soszyński et al. (2009, 2021)
LMC	ELL	Pawlak et al. (2016)
LMC	ECL	Pawlak et al. (2016)
SMC	OSARG	Soszyński et al. (2011)
SMC	Mira	Soszyński et al. (2011)
SMC	SRV	Soszyński et al. (2011)
SMC	LSP	Soszyński et al. (2011)
SMC	ELL	Pawlak et al. (2016)
SMC	ECL	Pawlak et al. (2016)
BLG	OSARG	Soszyński et al. (2013)
BLG	Mira	Soszyński et al. (2013)
BLG	SRV	Soszyński et al. (2013)
BLG	LSP	Soszyński et al. (2013)
BLG	ELL	Soszyński et al. (2016)
BLG	ECL	Soszyński et al. (2016)

Moreover, the PL diagrams show that those HBSs are a natural extension of sequence E for longer periods. In Figure 12, we present a close-up view of the RG HBSs in the PL diagrams. The color scale reflects the eccentricity of the system.

In the classical ellipsoidal variables, at a given brightness, the separation between stars in the system cannot be too small, because it may entail mass transfer via Roche-lobe overflow, and it cannot be too large, because then the amplitude of the brightness variations would be too slight to detect. Now, if we compare two systems with identical luminosities and periods, which indicates similar size of the semimajor axis, but one system has a circular orbit and the second one has an eccentric orbit, we can expect that the second system will be easier to detect because the minimal distance between components will be  $a(1 - e) < a$ , where  $a$  is the semimajor axis, thus the amplitude of the variations will be higher than for the first one. In Figure 12, we observe that the longer the period, the larger eccentricity is needed.

### 5.8. Detection of TEOs in OGLE HBSs

The results of our search for the TEOs are presented in Tables 2 and 3. In total, we were able to find 52 systems

**Figure 12.** Close-up view on the long period part of the  $P$ - $W_{JK}$  diagrams for stars located toward the GB (top panel) and in the LMC (lower panel). Note that for a given luminosity, HBSs with higher eccentric orbits have higher orbital periods.

out of 991 ( $\sim 5\%$ ) which exhibit at least a single TEO, while the total number of detected TEOs amounts to 78.

Figure 13 shows the compilation of frequency spectra of four sample OGLE HBSs with detected TEOs. The left-hand side of Figure 13 refers to one of the most prominent TEOs detected by us in OGLE-BLG-HB-0451, which out-of-periastron variability reveals the clear beating pattern between dominant  $n = 26$  and 30 TEOs. We also found evidence that 12 non-resonant frequencies present in four systems, namely OGLE-BLG-HB-0066, OGLE-BLG-HB-0157, OGLE-BLG-HB-0208, and OGLE-BLG-HB-0362 are possible non-harmonic TEOs formed via the parametric instability NLMC mechanism. We did not detect their corresponding "mother" modes, however, this can be explained with amplitudes below the detection limit (typically between 0.2 and 3.0 mmag in analyzed OGLE light curves).

Additionally, in Tables 2 and 3 we have marked those systems which, in parallel to the TEOs, also show a well-pronounced intrinsic coherent variability. This may help in future research about the interaction between tides and intrinsic pulsations. Do tidal interactions suppress self-excited pulsations or do they not have a major im-

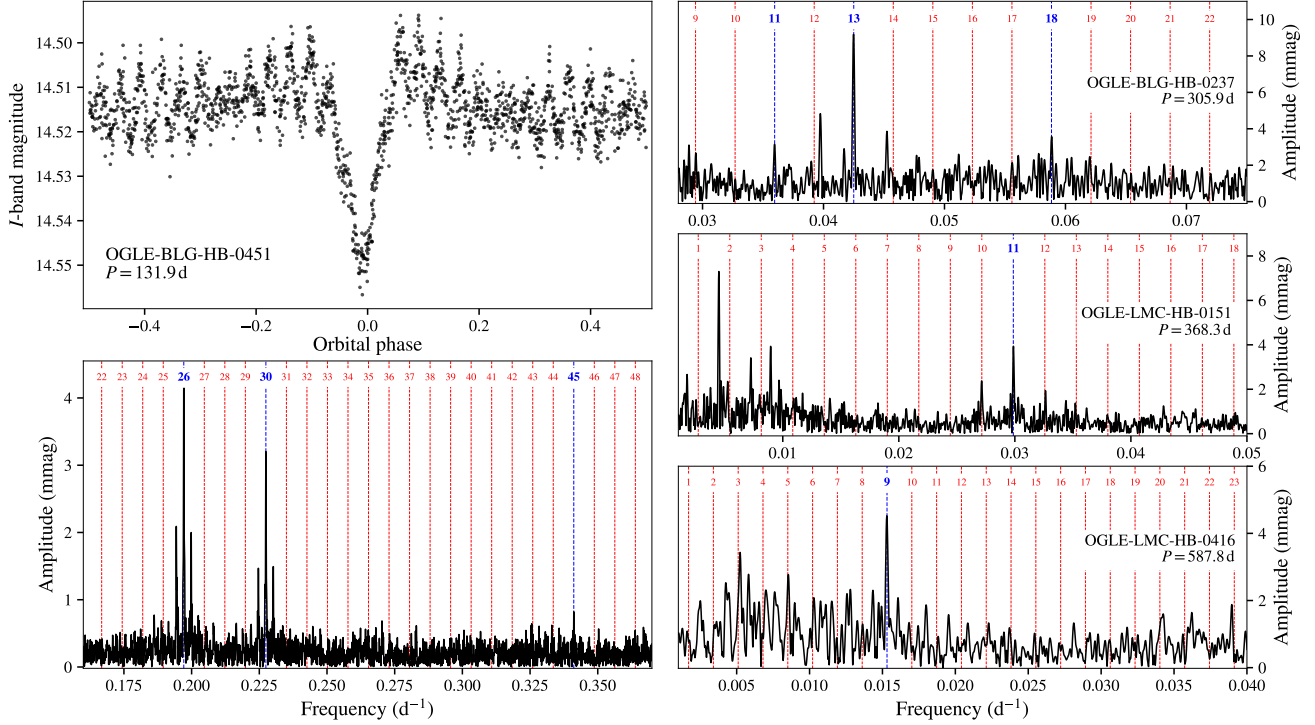


**Figure 13.** Sample of TEOs detected in the OGLE HBSs. (Top left): The phase-folded light curve of OGLE-BLG-HB-0451. Zero phase corresponds to the periastron passage. Both, the heartbeat (around the periastron) and high-amplitude TEOs (across the entire phase range) are clearly visible; (Bottom left): The Fourier frequency spectrum of the light curve of OGLE-BLG-HB-0451 (shown in the top left panel) after subtraction of the best-fitting Kumar’s model. The vertical dashed lines mark the position of consecutive harmonics of the orbital frequency. Multiple TEOs at  $n = 26, 30$ , and  $45$  are highlighted with vertical blue lines. Side peaks around TEO  $n = 26$  and  $30$  are due to aliasing; (Right): The Fourier frequency spectra analogous to the spectrum presented in the bottom left panel, but for the OGLE-BLG-HB-0237, OGLE-LMC-HB-0151, and OGLE-LMC-HB-0416 systems.

pect on them (e.g., Springer & Shaviv 2013, Fuller et al. 2020)? The cases in which we did not detect any significant coherent variability are also interesting because of the question raised above.

The presented sample of TEOs is the largest homogeneous sample of this kind known so far, which allows us to statistically investigate the dependence between parameters like  $n$ ,  $e$ , and the amplitude of a TEO. From a theoretical point of view, greater eccentricities should favor TEOs with higher  $n$ ’s. This intuitive fact is dictated by the equivalent of dimensionless Hansen coefficient,  $X_{nm}$ , which assuming spin-orbit alignment in the system, equals  $X_{nm} = W_{lm}F_{nm}$ .  $F_{nm}$  is given by the following expression (Fuller 2017, his Equation 5)

$$F_{nm} = \frac{1}{\pi} \int_0^\pi \frac{\cos[n(E - e \sin E) - m\varphi(t)]}{(1 - e \cos E)^l} dE. \quad (16)$$

$W_{lm}$  is a constant depending only on the geometry of a given mode. Keeping the assumption about spin-orbit alignment,  $W_{20} = -(\pi/5)^{1/2}$  while  $W_{22} = (3\pi/10)^{1/2}$ . Figure 14 (middle and lower panel) shows the evolution

of  $\log(|X_{nm}|)$  with increasing eccentricity for quadruple modes with  $m = 0$  or  $2$ . The former ones have maximal values of  $X_{nm}$  at  $n = 1$ , regardless of the eccentricity. The latter modes characterize with  $X_{nm}$  which peaks at  $n > 1$ . Moreover, the position of maximum moves away to higher  $n$ ’s with the increasing eccentricity.

The empirical relation between  $n$  of a TEO and the eccentricity can be seen in the upper panel of Figure 14. First of all, theoretical predictions about the positive correlation between  $n$  and  $e$ , which we described above, are reflected in the obtained empirical distribution of TEOs. Next, although Figure 14 contains 62 TEOs plotted on the  $e$ - $n$  plane, it seems plausible that the graph reveals the presence of two separated groups of TEOs. They have been schematically marked by us with shaded regions. It is possible that the significant shift between maximal values of  $X_{nm}$  for quadruple modes with  $m = 0$  and  $2$  propagates on the empirical distribution. Finally, we did not find any clear relation between the amplitude of a TEO,  $e$ , and  $n$ , but yet we would like to emphasize that TEOs are not restricted to strongly eccentric binaries. In our sample, we can still observe high-amplitude

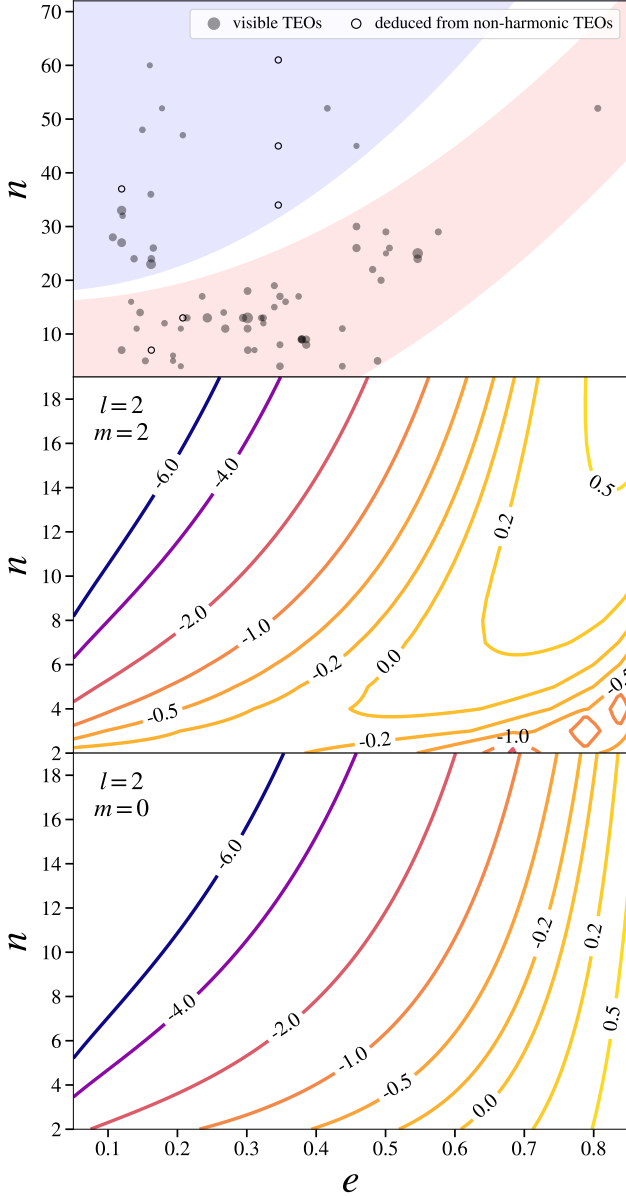


**Figure 14.** (Top): Empirical relation between the harmonic number of the TEOs detected in the OGLE HBSs (Tables 2 and 3) and their estimated eccentricities. Directly detected TEOs are denoted with filled circles. The higher the amplitude of a TEO, the bigger a circle. Empty circles correspond to TEOs deduced from the presence of "daughter" non-harmonic TEOs. The red and blue shaded regions suggest the division into two groups of TEOs, which we discuss in detail in the text (Section 5.8); (Middle): Contour plot of  $\log(|X_{nm}|)$  values versus  $n$  and  $e$  for  $l = 2$ ,  $m = 2$  modes; (Bottom): The same as middle panel but for  $m = 0$  modes.

TEOs even in systems with  $e \approx 0.1$ . Some of these TEOs are related to the surprisingly high harmonics of the orbital frequency, despite the low value of  $e$ , what awaits a theoretical explanation.

## 6. CONCLUSIONS

We have presented an analysis of the HBSs sample from the OCVS (Wrona et al. 2021), based on their photometric properties. The sample consists of 512 and 479 HBSs located toward the GB and MCs, respectively. An  $I$ -band light curve variation has been modeled using a simple analytic model of the tidal deformation in the binary during periastron passage described in Kumar et al. (1995). The Kumar's model parameters for all HBSs were estimated using the `emcee` Python package, which provides the fitting with the MCMC method. We have presented the distribution of orbital parameters  $e$ ,  $i$ , and  $\omega$ . The  $\omega$  can be described by a flat distribution, as expected, while the  $i$  by the normal distribution around  $65^\circ$ , which is a rather observational bias effect, and additional artificial peak near  $90^\circ$ . The majority of our HBSs have orbits with low eccentricity ( $0.1 \lesssim e \lesssim 0.35$ ), but we also observe orbits with very high eccentricity where  $e \gtrsim 0.5$ .

We have shown CMDs and HR diagrams, which indicate that HBSs, similar to the ellipsoidal and eclipsing binaries, are variables that do not belong to specific evolutionary status or position on those diagrams. The most visible are two groups of HBSs. The first group of fewer than 100 systems consist of an early-type primary star lying on the MS or Hertzsprung gap and the second group of about 900 systems contains most probably an RGB or AGB star. By comparing positions of HBSs on the HR diagram to the theoretical evolutionary tracks, we see a wide range of the initial mass of the primary, from less than  $1 M_\odot$  to as high as  $40 M_\odot$ . However, bearing in mind that we assume here a separate evolution, which is most likely not the case for evolved RG stars.

Cool and hot HBSs distinctly differ in the period distribution and slightly in the flux variation amplitudes. The majority of hot HBSs have orbital periods in a range from a few days to 30-40 days, while the RG part of the sample is dominated by long-period binaries with the median value of about one year. In the case of the  $I$ -band amplitude, the mean value is similar for both groups, but the scatter is larger for hot stars.

Like the classical ellipsoidal variables, the RG HBSs also group on the PL diagrams, extending the sequence E to longer periods at a given brightness, which is strong evidence confirming their binary nature. Moreover, thanks to the large number of HBSs, we proved



that for a given brightness, the higher the eccentricity, the longer the period.

Using *I*-band photometry, we also performed time-series analysis and we found TEOs in 52 objects with a total number of 76 modes. Those oscillations occur at harmonics of orbital frequencies in the range between 4 and 79. We also provide evidence that some of them may formed due to NLMC. Thanks to this relatively large and homogeneous sample of TEOs, we were able to construct for the first time a diagram showing the positive correlation between TEO's  $n$  and eccentricity, as predicted by theory.

#### ACKNOWLEDGMENT

We thank Prof. Igor Soszyński for the comments that helped to improve this manuscript. This work has been supported by the Polish National Science Centre grant OPUS 16 no. 2018/31/B/ST9/00334 and MAESTRO 8 no. 2016/22/A/ST9/00009. PKS acknowledges support from the Polish National Science Centre grant PRE-

LUDIUM 18 no. 2019/35/N/ST9/03805. This publication makes use of data products from the Two Micron All Sky Survey, which is a joint project of the University of Massachusetts and the Infrared Processing and Analysis Center/California Institute of Technology, funded by the National Aeronautics and Space Administration and the National Science Foundation. The Infrared Survey Facility (IRSF) project is a collaboration between Nagoya University and the South African Astronomical Observatory (SAAO) supported by the Grants-in-Aid for Scientific Research on Priority Areas (A) (no. 10147207 and no. 10147214) and Optical & Near-Infrared Astronomy Inter-University Cooperation Program, from the Ministry of Education, Culture, Sports, Science and Technology (MEXT) of Japan and the National Research Foundation (NRF) of South Africa. This research also made use of **ASTROPY**, a community-developed core Python package for Astronomy ([Astropy Collaboration et al. 2018](#)).

**Table 2.** TEOs detected in OGLE HBSs located towards the GB.

OGLE ID	Frequency (d <sup>-1</sup> )	Amplitude (mmag)	$n$	$\Delta n$	$S/N$
OGLE-BLG-HB-0066 <sup>ICV</sup>	0.069502(8)	6.0(5)	33	-0.006(9)	9.51
	0.056926(10)	5.1(6)	27	+0.023(9)	8.14
	0.014769(13)	3.4(5)	7	+0.011(7)	5.49
	0.059262(10)*	4.6(5)	37	-0.012(11)	7.41
	0.018654(12)*	3.9(5)			6.21
OGLE-BLG-HB-0081 <sup>ICV</sup>	0.048188(9)	1.94(26)	52	+0.002(9)	5.80
OGLE-BLG-HB-0091 <sup>ICV</sup>	0.044299(9)	7.2(8)	23	+0.00005±0.01	8.43
OGLE-BLG-HB-0095 <sup>ICV</sup>	0.123049(14)	1.17(17)	32	+0.02(7)	5.45
OGLE-BLG-HB-0143	0.202440(9)	2.31(25)	22	-0.0040(20)	7.10
OGLE-BLG-HB-0145 <sup>ICV</sup>	0.034637(13)	0.92(6)	11	+0.001(4)	14.21
OGLE-BLG-HB-0147 <sup>ICV</sup>	0.037320(13)	1.28(18)	17	-0.002(6)	5.81
OGLE-BLG-HB-0156	0.0791056(28)	2.01(6)	29	-0.0013(12)	27.02
OGLE-BLG-HB-0157 <sup>ICV</sup>	0.051040(9)*	3.9(4)	61	+0.008±0.015	9.52
	0.054405(9)*	3.6(3)			8.77
	0.037978(7)*	4.9(3)	34	+0.007±0.011	11.76
	0.020775(12)*	2.7(3)			6.52
	0.037362(8)*	3.9(3)	45	-0.0009±0.012	9.75
	0.040414(9)*	3.5(3)			8.58
OGLE-BLG-HB-0160 <sup>ICV</sup>	0.024130(12)	0.75(6)	7	+0.011(4)	10.23

**Table 2** *continued*

**Table 2** (*continued*)

OGLE ID	Frequency (d <sup>-1</sup> )	Amplitude (mmag)	<i>n</i>	$\Delta n$	<i>S/N</i>
OGLE-BLG-HB-0208 <sup>ICV</sup>	0.146553(19)	1.10(21)	47	+0.008(9)	4.15
	0.018556(9)*	2.09(22)	13	-0.002(5)	7.88
	0.021967(13)*	1.65(21)			6.20
OGLE-BLG-HB-0209 <sup>ICV</sup>	0.055979(14)	0.70(9)	25	+0.020(7)	7.77
OGLE-BLG-HB-0211 <sup>ICV</sup>	0.077900(17)	0.71(13)	16	-0.007(4)	4.25
OGLE-BLG-HB-0225 <sup>ICV</sup>	0.017026(9)	0.70(5)	5	-0.0072(28)	13.26
	0.020405(11)	0.65(5)	6	+0.001(3)	12.29
OGLE-BLG-HB-0234 <sup>ICV</sup>	0.007065(9)	1.55(14)	4	-0.010(5)	8.66
	0.019491(9)	1.60(15)	11	+0.008(6)	8.93
OGLE-BLG-HB-0237 <sup>ICV</sup>	0.042487(5)	9.4(5)	13	-0.0035(18)	14.68
	0.035964(13)	3.4(5)	11	+0.001(4)	5.38
	0.058859(13)	3.3(5)	18	+0.005(4)	5.20
OGLE-BLG-HB-0261 <sup>ICV</sup>	0.372014(14)	0.55(8)	60	+0.004(4)	5.59
OGLE-BLG-HB-0273 <sup>ICV</sup>	0.041733(8)	0.68(7)	11	-0.0096(23)	8.12
	0.015196(9)	0.61(7)	4	+0.0020(25)	7.23
OGLE-BLG-HB-0286 <sup>ICV</sup>	0.207209(12)	0.65(9)	52	+0.009(5)	7.31
OGLE-BLG-HB-0298	0.0582328(27)	6.31(20)	13	-0.0054(7)	33.81
OGLE-BLG-HB-0310 <sup>ICV</sup>	0.065275(6)	3.55(23)	28	+0.019(7)	12.54
OGLE-BLG-HB-0315	0.12390(4)	1.51(22)	52	+0.04(4)	5.57
OGLE-BLG-HB-0346 <sup>ICV</sup>	0.070270(7)	1.94(15)	13	+0.0006±0.0016	10.83
	0.064861(14)	0.98(14)	12	-0.00022±0.0028	5.48
OGLE-BLG-HB-0357 <sup>ICV</sup>	0.196011(18)	1.32(16)	48	+0.018(7)	7.95
OGLE-BLG-HB-0362 <sup>ICV</sup>	0.071917(6)	2.76(13)	24	-0.0031(24)	21.71
	0.009237(7)*	2.38(13)	7	-0.007(4)	18.76
	0.011720(9)*	1.89(13)			14.90
OGLE-BLG-HB-0435 <sup>ICV</sup>	0.032134(9)	2.94(27)	14	+0.008(6)	8.86
OGLE-BLG-HB-0451	0.197094(3)	4.04(13)	26	-0.0016(12)	23.38
	0.227416(4)	3.04(14)	30	-0.0019(15)	17.56
	0.341157(17)	0.75(14)	45	+0.002(3)	4.31
OGLE-BLG-HB-0463	0.069864(9)	1.46(13)	16	-0.0002±0.0023	9.06
OGLE-BLG-HB-0486	0.020009(8)	2.79(26)	4	+0.0010(17)	8.41
	0.084990(9)	2.50(26)	17	-0.0050(23)	7.56
	0.040022(13)	1.90(26)	8	+0.0030(26)	5.72

NOTE—<sup>ICV</sup> Well-pronounced intrinsic coherent variability coexisting with TEOs. \* Possible non-harmonic TEOs present due to the NLMC. In such a case, the pair of frequencies denoted with \* and enclosed in a brace are suspected to be "daughter" modes of harmonic "mother" TEO with *n* provided after the brace.

**Table 3.** The same as Table 2 but for OGLE HBSs located in the MCs.

OGLE ID	Frequency (d <sup>-1</sup> )	Amplitude (mmag)	<i>n</i>	$\Delta n$	<i>S/N</i>
OGLE-LMC-HB-0006	0.059295(18)	1.29(25)	12	-0.003(4)	4.29
OGLE-LMC-HB-0044 <sup>ICV</sup>	0.037458(16)	1.72(26)	26	+0.007±0.014	4.87
OGLE-LMC-HB-0101 <sup>ICV</sup>	0.051118(20)	1.94(25)	19	+0.003±0.010	6.31
	0.040375(29)	1.35(24)	15	+0.009±0.012	4.37
OGLE-LMC-HB-0109 <sup>ICV</sup>	0.035508(11)	1.60(17)	17	+0.010(12)	7.52
OGLE-LMC-HB-0151 <sup>ICV</sup>	0.029874(4)	4.16(24)	11	+0.0025(18)	13.71
OGLE-LMC-HB-0152 <sup>ICV</sup>	0.040469(17)	2.6(4)	24	+0.027(18)	5.87
OGLE-LMC-HB-0207	1.341280(9)	1.51(23)	9	-0.00015(7)	5.18
OGLE-LMC-HB-0208 <sup>ICV</sup>	0.036602(14)	1.9(3)	29	-0.003±0.015	4.86
OGLE-LMC-HB-0209 <sup>ICV</sup>	0.040007(9)	1.48(21)	14	-0.003(3)	5.67
OGLE-LMC-HB-0221 <sup>ICV</sup>	0.076413(9)	1.77(24)	36	-0.006(8)	6.12
OGLE-LMC-HB-0223 <sup>ICV</sup>	0.059357(15)	2.6(4)	26	+0.003±0.014	5.76
OGLE-LMC-HB-0231 <sup>ICV</sup>	0.076427(9)	1.62(26)	79	+0.008±0.016	5.20
OGLE-LMC-HB-0236 <sup>ICV</sup>	0.028232(5)	3.88(29)	13	+0.0004±0.0023	11.03
OGLE-LMC-HB-0254	0.761545(14)	8.8(8)	25	+0.0009(6)	8.73
	0.731068(27)	4.7(8)	24	+0.0004(9)	4.66
OGLE-LMC-HB-0287	0.032715(15)	3.5(5)	9	-0.005(4)	5.57
OGLE-LMC-HB-0308	0.149763(9)	3.1(3)	5	-0.0006(3)	7.54
OGLE-LMC-HB-0350	1.413994(6)	2.99(20)	7	-0.00017(6)	12.77
OGLE-LMC-HB-0351	0.041056(9)	1.47(19)	13	-0.004(3)	6.10
OGLE-LMC-HB-0385 <sup>ICV</sup>	0.028620(19)	2.21(25)	20	+0.00012±0.014	7.06
OGLE-LMC-HB-0416 <sup>ICV</sup>	0.015303(8)	4.4(4)	9	-0.005(6)	8.92
OGLE-SMC-HB-0015	0.157140(8)	3.3(4)	9	+0.0005(4)	6.75
	0.139663(7)	3.9(4)	8	-0.0006(4)	8.10
OGLE-SMC-HB-0018	0.089935(13)	2.4(4)	13	-0.0070(20)	5.17
OGLE-SMC-HB-0019	0.161628(7)	2.00(22)	5	+0.00027(21)	7.35

NOTE—<sup>ICV</sup> Well-pronounced intrinsic coherent variability coexisting with TEOs.

## REFERENCES

- Akima, H. 1970, J. ACM, 17, 589–602, doi: [10.1145/321607.321609](https://doi.org/10.1145/321607.321609)
- Alard, C., & Lupton, R. H. 1998, ApJ, 503, 325, doi: [10.1086/305984](https://doi.org/10.1086/305984)

- Astropy Collaboration, Price-Whelan, A. M., Sipőcz, B. M., et al. 2018, *AJ*, 156, 123, doi: [10.3847/1538-3881/aabc4f](https://doi.org/10.3847/1538-3881/aabc4f)
- Beck, P. G., Hambleton, K., Vos, J., et al. 2014, *A&A*, 564, A36, doi: [10.1051/0004-6361/201322477](https://doi.org/10.1051/0004-6361/201322477)
- Bertelli, G., Girardi, L., Marigo, P., & Nasi, E. 2008, *A&A*, 484, 815, doi: [10.1051/0004-6361:20079165](https://doi.org/10.1051/0004-6361:20079165)
- Bessell, M. S., Castelli, F., & Plez, B. 1998, *A&A*, 333, 231
- Borucki, W. J., Koch, D., Basri, G., et al. 2010, *Science*, 327, 977, doi: [10.1126/science.1185402](https://doi.org/10.1126/science.1185402)
- Burkert, J., Quataert, E., Arras, P., & Weinberg, N. N. 2012, *MNRAS*, 421, 983, doi: [10.1111/j.1365-2966.2011.20344.x](https://doi.org/10.1111/j.1365-2966.2011.20344.x)
- Castelli, F., & Kurucz, R. L. 2003, in *Modelling of Stellar Atmospheres*, ed. N. Piskunov, W. W. Weiss, & D. F. Gray, Vol. 210, A20. <https://arxiv.org/abs/astro-ph/0405087>
- Chen, Y., Girardi, L., Fu, X., et al. 2019, *A&A*, 632, A105, doi: [10.1051/0004-6361/201936612](https://doi.org/10.1051/0004-6361/201936612)
- Choi, J., Dotter, A., Conroy, C., et al. 2016, *ApJ*, 823, 102, doi: [10.3847/0004-637X/823/2/102](https://doi.org/10.3847/0004-637X/823/2/102)
- Conroy, K. E., Kochoska, A., Hey, D., et al. 2020, *ApJS*, 250, 34, doi: [10.3847/1538-4365/abb4e2](https://doi.org/10.3847/1538-4365/abb4e2)
- Dotter, A. 2016, *ApJS*, 222, 8, doi: [10.3847/0067-0049/222/1/8](https://doi.org/10.3847/0067-0049/222/1/8)
- Dutra, C. M., Santiago, B. X., & Bica, E. 2002, *A&A*, 381, 219, doi: [10.1051/0004-6361:20011541](https://doi.org/10.1051/0004-6361:20011541)
- Dziembowski, W. 1982, *AcA*, 32, 147
- Foreman-Mackey, D., Hogg, D. W., Lang, D., & Goodman, J. 2013, *PASP*, 125, 306, doi: [10.1086/670067](https://doi.org/10.1086/670067)
- Fuller, J. 2017, *MNRAS*, 472, 1538, doi: [10.1093/mnras/stx2135](https://doi.org/10.1093/mnras/stx2135)
- Fuller, J., Kurtz, D. W., Handler, G., & Rappaport, S. 2020, *MNRAS*, 498, 5730, doi: [10.1093/mnras/staa2376](https://doi.org/10.1093/mnras/staa2376)
- Fuller, J., & Lai, D. 2012, *MNRAS*, 420, 3126, doi: [10.1111/j.1365-2966.2011.20237.x](https://doi.org/10.1111/j.1365-2966.2011.20237.x)
- Guo, Z. 2020, *ApJ*, 896, 161, doi: [10.3847/1538-4357/ab911f](https://doi.org/10.3847/1538-4357/ab911f)
- Guo, Z. 2021, *Frontiers in Astronomy and Space Sciences*, 8, 67, doi: [10.3389/fspas.2021.663026](https://doi.org/10.3389/fspas.2021.663026)
- Guo, Z., Shporer, A., Hambleton, K., & Isaacson, H. 2020, *ApJ*, 888, 95, doi: [10.3847/1538-4357/ab58c2](https://doi.org/10.3847/1538-4357/ab58c2)
- Hambleton, K., Kurtz, D. W., Prša, A., et al. 2016, *MNRAS*, 463, 1199, doi: [10.1093/mnras/stw1970](https://doi.org/10.1093/mnras/stw1970)
- Hambleton, K., Fuller, J., Thompson, S., et al. 2018, *MNRAS*, 473, 5165, doi: [10.1093/mnras/stx2673](https://doi.org/10.1093/mnras/stx2673)
- Handler, G., Balona, L. A., Shobbrook, R. R., et al. 2002, *MNRAS*, 333, 262, doi: [10.1046/j.1365-8711.2002.05295.x](https://doi.org/10.1046/j.1365-8711.2002.05295.x)
- Harris, J., & Zaritsky, D. 2009, *AJ*, 138, 1243, doi: [10.1088/0004-6256/138/5/1243](https://doi.org/10.1088/0004-6256/138/5/1243)
- Hauschildt, P. H., Baron, E., & Allard, F. 1997, *ApJ*, 483, 390, doi: [10.1086/304233](https://doi.org/10.1086/304233)
- Horvat, M., Conroy, K. E., Pablo, H., et al. 2018, *ApJS*, 237, 26, doi: [10.3847/1538-4365/aacd0f](https://doi.org/10.3847/1538-4365/aacd0f)
- Houdashelt, M. L., Bell, R. A., & Sweigart, A. V. 2000, *AJ*, 119, 1448, doi: [10.1086/301243](https://doi.org/10.1086/301243)
- Husser, T. O., Wende-von Berg, S., Dreizler, S., et al. 2013, *A&A*, 553, A6, doi: [10.1051/0004-6361/201219058](https://doi.org/10.1051/0004-6361/201219058)
- Hut, P. 1980, *A&A*, 92, 167
- Jayasinghe, T., Stanek, K. Z., Kochanek, C. S., et al. 2019, *MNRAS*, 489, 4705, doi: [10.1093/mnras/stz2460](https://doi.org/10.1093/mnras/stz2460)
- Jayasinghe, T., Kochanek, C. S., Strader, J., et al. 2021, *arXiv e-prints*, arXiv:2104.13925. <https://arxiv.org/abs/2104.13925>
- Jones, D., Conroy, K. E., Horvat, M., et al. 2020, *ApJS*, 247, 63, doi: [10.3847/1538-4365/ab7927](https://doi.org/10.3847/1538-4365/ab7927)
- Kato, D., Nagashima, C., Nagayama, T., et al. 2007, *PASJ*, 59, 615, doi: [10.1093/pasj/59.3.615](https://doi.org/10.1093/pasj/59.3.615)
- Kirk, B., Conroy, K., Prša, A., et al. 2016, *AJ*, 151, 68, doi: [10.3847/0004-6256/151/3/68](https://doi.org/10.3847/0004-6256/151/3/68)
- Kołaczek-Szymański, P. A., Pigulski, A., Michalska, G., Moździerski, D., & Różański, T. 2021, *A&A*, 647, A12, doi: [10.1051/0004-6361/202039553](https://doi.org/10.1051/0004-6361/202039553)
- Kumar, P., Ao, C. O., & Quataert, E. J. 1995, *ApJ*, 449, 294, doi: [10.1086/176055](https://doi.org/10.1086/176055)
- Maceroni, C., Montalbán, J., Michel, E., et al. 2009, *A&A*, 508, 1375, doi: [10.1051/0004-6361/200913311](https://doi.org/10.1051/0004-6361/200913311)
- Massey, P. 2002, *ApJS*, 141, 81, doi: [10.1086/338286](https://doi.org/10.1086/338286)
- Massey, P., Garmany, C. D., Silkey, M., & Degioia-Eastwood, K. 1989, *AJ*, 97, 107, doi: [10.1086/114961](https://doi.org/10.1086/114961)
- Morris, S. L. 1985, *ApJ*, 295, 143, doi: [10.1086/163359](https://doi.org/10.1086/163359)
- Nataf, D. M., Gould, A., Fouqué, P., et al. 2013, *ApJ*, 769, 88, doi: [10.1088/0004-637X/769/2/88](https://doi.org/10.1088/0004-637X/769/2/88)
- Nicholls, C. P., & Wood, P. R. 2012, *MNRAS*, 421, 2616, doi: [10.1111/j.1365-2966.2012.20492.x](https://doi.org/10.1111/j.1365-2966.2012.20492.x)
- Nicholls, C. P., Wood, P. R., & Cioni, M. R. L. 2010, *MNRAS*, 405, 1770, doi: [10.1111/j.1365-2966.2010.16548.x](https://doi.org/10.1111/j.1365-2966.2010.16548.x)
- Nie, J. D., & Wood, P. R. 2014, *AJ*, 148, 118, doi: [10.1088/0004-6256/148/6/118](https://doi.org/10.1088/0004-6256/148/6/118)
- Nie, J. D., Wood, P. R., & Nicholls, C. P. 2012, *MNRAS*, 423, 2764, doi: [10.1111/j.1365-2966.2012.21087.x](https://doi.org/10.1111/j.1365-2966.2012.21087.x)
- . 2017, *ApJ*, 835, 209, doi: [10.3847/1538-4357/835/2/209](https://doi.org/10.3847/1538-4357/835/2/209)
- Pawlak, M., Soszyński, I., Udalski, A., et al. 2016, *AcA*, 66, 421. <https://arxiv.org/abs/1612.06394>
- Paxton, B., Bildsten, L., Dotter, A., et al. 2011, *ApJS*, 192, 3, doi: [10.1088/0067-0049/192/1/3](https://doi.org/10.1088/0067-0049/192/1/3)
- Paxton, B., Cantiello, M., Arras, P., et al. 2013, *ApJS*, 208, 4, doi: [10.1088/0067-0049/208/1/4](https://doi.org/10.1088/0067-0049/208/1/4)



- Pietrukowicz, P., Kozłowski, S., Skowron, J., et al. 2015, *ApJ*, 811, 113, doi: [10.1088/0004-637X/811/2/113](https://doi.org/10.1088/0004-637X/811/2/113)
- Pietrzyński, G., Graczyk, D., Gallenne, A., et al. 2019, *Nature*, 567, 200, doi: [10.1038/s41586-019-0999-4](https://doi.org/10.1038/s41586-019-0999-4)
- Pourbaix, D., Tokovinin, A. A., Batten, A. H., et al. 2004, *A&A*, 424, 727, doi: [10.1051/0004-6361:20041213](https://doi.org/10.1051/0004-6361:20041213)
- Prša, A., & Zwitter, T. 2005, *ApJ*, 628, 426, doi: [10.1086/430591](https://doi.org/10.1086/430591)
- Prša, A., Harmanec, P., Torres, G., et al. 2016a, *AJ*, 152, 41, doi: [10.3847/0004-6256/152/2/41](https://doi.org/10.3847/0004-6256/152/2/41)
- Prša, A., Conroy, K. E., Horvat, M., et al. 2016b, *ApJS*, 227, 29, doi: [10.3847/1538-4365/227/2/29](https://doi.org/10.3847/1538-4365/227/2/29)
- Skowron, D. M., Skowron, J., Udalski, A., et al. 2021, *ApJS*, 252, 23, doi: [10.3847/1538-4365/abcb81](https://doi.org/10.3847/1538-4365/abcb81)
- Skowron, J., Udalski, A., Kozłowski, S., et al. 2016, *AcA*, 66, 1. <https://arxiv.org/abs/1604.01966>
- Skrutskie, M. F., Cutri, R. M., Stiening, R., et al. 2006, *AJ*, 131, 1163, doi: [10.1086/498708](https://doi.org/10.1086/498708)
- Soszyński, I., Udalski, A., Kubiak, M., et al. 2004, *AcA*, 54, 347. <https://arxiv.org/abs/astro-ph/0412505>
- Soszyński, I., Udalski, A., Szymański, M. K., et al. 2009, *AcA*, 59, 239. <https://arxiv.org/abs/0910.1354>
- . 2011, *AcA*, 61, 217. <https://arxiv.org/abs/1109.1143>
- . 2013, *AcA*, 63, 21. <https://arxiv.org/abs/1304.2787>
- Soszyński, I., Pawlak, M., Pietrukowicz, P., et al. 2016, *AcA*, 66, 405. <https://arxiv.org/abs/1701.03105>
- Soszyński, I., Olechowska, A., Ratajczak, M., et al. 2021, *ApJL*, 911, L22, doi: [10.3847/2041-8213/abf3c9](https://doi.org/10.3847/2041-8213/abf3c9)
- Springer, O. M., & Shaviv, N. J. 2013, *Monthly Notices of the Royal Astronomical Society*, 434, 1869, doi: [10.1093/mnras/stt1041](https://doi.org/10.1093/mnras/stt1041)
- Storm, J., Gieren, W., Fouqué, P., et al. 2011, *A&A*, 534, A94, doi: [10.1051/0004-6361/201117155](https://doi.org/10.1051/0004-6361/201117155)
- Thompson, S. E., Everett, M., Mullally, F., et al. 2012, *ApJ*, 753, 86, doi: [10.1088/0004-637X/753/1/86](https://doi.org/10.1088/0004-637X/753/1/86)
- Udalski, A., Szymański, M. K., & Szymański, G. 2015, *AcA*, 65, 1. <https://arxiv.org/abs/1504.05966>
- Welsh, W. F., Orosz, J. A., Aerts, C., et al. 2011, *ApJS*, 197, 4, doi: [10.1088/0067-0049/197/1/4](https://doi.org/10.1088/0067-0049/197/1/4)
- Wilson, R. E. 1990, *ApJ*, 356, 613, doi: [10.1086/168867](https://doi.org/10.1086/168867)
- Wilson, R. E., & Devinney, E. J. 1971, *ApJ*, 166, 605, doi: [10.1086/150986](https://doi.org/10.1086/150986)
- Wood, P. R., Alcock, C., Allsman, R. A., et al. 1999, in *Asymptotic Giant Branch Stars*, ed. T. Le Bertre, A. Lebre, & C. Waelkens, Vol. 191, 151
- Woźniak, P. R. 2000, *AcA*, 50, 421. <https://arxiv.org/abs/astro-ph/0012143>
- Zahn, J. P. 1970, *A&A*, 4, 452
- . 1975, *A&A*, 41, 329
- Zaritsky, D., Harris, J., Thompson, I. B., & Grebel, E. K. 2004, *AJ*, 128, 1606, doi: [10.1086/423910](https://doi.org/10.1086/423910)